# Effect of Ag addition on the precipitation evolution and interfacial segregation for Al-Mg-Si alloy

Yaoyao Weng [a, 1], Lipeng Ding [c, d, 1], Zezhong Zhang [d,g], Zhihong Jia [a, b, *], Boyang Wen [a], Yingying Liu [a, b], Shinji Muraishi [e], Yanjun Li [f], Qing Liu [a, b, **]

[a] *International Joint laboratory for Light Alloys (Ministry of Education), College of Materials Science and Engineering, Chongqing University, Chongqing 400044, China*

[b] *Electron Microscopy Center of Chongqing University, Chongqing 400044, China*

[c] *Université catholique de Louvain, Institute of Mechanics, Materials and Civil Engineering, IMAP, 1348 Louvain-la-Neuve, Belgium*

[d] *Electron Microscopy for Materials Science (EMAT), Department of Physics, University of Antwerp, Groenenborgerlaan 171, B-2020, Belgium*

[e] *Department of Metallurgy and Ceramics Science, Tokyo Institute of Technology, 2-12-1 Meguro-ku, Tokyo 152-8552, Japan*

[f] *Department of Materials Science and Engineering, Norwegian University of Science and Technology, Alfred Getz vei 2b, N-7491 Trondheim, Norway*

[g] Department of Materials, University of Oxford, 16 Parks Road, Oxford OX1 3PH, United Kingdom.

[*] Corresponding author. International Joint laboratory for Light Alloys (Ministry of Education), College of Materials Science and Engineering, Chongqing University, Chongqing 400044, China.

[**] Corresponding author. International Joint laboratory for Light Alloys (Ministry of Education), College of Materials Science and Engineering, Chongqing University, Chongqing 400044, China.

E-mail addresses: zhihongjia@cqu.edu.cn (Zhihong Jia), qingliu@cqu.edu.cn (Qing Liu).

[1] These authors contributed equally to this work.

## Abstract:

The effect of Ag addition on the precipitation evolution and interfacial segregation for Al-Mg-Si alloys was systematically investigated by atomic resolution high-angle annular dark-field scanning transmission electron microscopy (HAADF-STEM), atom probe tomography (APT) and density functional theory (DFT) calculation. At the early aging stage, Ag atoms could enter clusters and refine the distribution of these clusters. Then, Ag atoms preferentially segregate at the GP zone/α-Al and β"/α-Al interfaces at the peak aging stage

by the replacement of Al atoms in FCC matrix. With prolonging aging time, Ag atoms generally incorporate into the interior of β" precipitate, facilitating the formation of QP lattice (a hexagonal network of Si atomic columns) and the local symmetry substructures, Ag sub-unit (1) and Ag sub-unit (2). At the over-aged stage, the Ag sub-unit (1) and Ag sub-unit (2) could transform to the $\beta'_{Ag}$ (i.e. $\beta'_{Ag1}$ and $\beta'_{Ag2}$.) and $Q'_{Ag}$ unit cells, respectively. All the precipitates at the over-aging stage have a composite and disordered structure due to the coexistence of different unit cells ($\beta'_{Ag1}$, $\beta'_{Ag2}$, $Q'_{Ag}$ and β′) and the non-periodic arrangement of Ag atoms within the precipitate. In the equilibrium stage, the incorporated Ag atoms in the precipitates release into the α-Al matrix as solute atoms or form Ag particles. In general, Ag atoms undergo a process of "segregate at the precipitate/matrix interface → incorporate into the interior of precipitate → release into the α-Al matrix" during the precipitation for Al-Mg-Si-Ag alloys. Besides, Ag segregation is found at the interfaces of almost all metastable phases (including GP zone, β″, β′/ $\beta'_{Ag}$ phase) in Al-Mg-Si-Ag alloys. The Ag segregation at the β′/α-Al interface could increase the length/diameter ratio of β′ phase and thus promote the additional strengthening potential of these alloys. These findings provide a new route for precipitation hardening by promoting the nucleation and morphology evolution of precipitates.

**Keywords:** Al-Mg-Si alloy; Ag segregation; precipitation; atomic-resolution HAADF-STEM; First-principles calculation;

# 1. Introduction

Al-Mg-Si alloys are increasingly attractive as a candidate in automotive industry because of its high strength/weight ratio, good formability and corrosion resistance properties [1-3]. These alloys are strengthened by the formation of nano-sized, semi-coherent metastable precipitates at elevated temperature. The precipitation sequence of Al-Mg-Si alloys is usually considered as [4-10]:

$$\text{SSSS} \rightarrow \text{atomic clusters} \rightarrow \text{GP zones} \rightarrow \beta'' \rightarrow \text{U1, U2, B', } \beta' \rightarrow \beta, \text{Si}$$

SSSS represents the supersaturated solid solution. Clusters and GP zones are formed at the early stage of aging and coherent with the α-Al matrix. The needle-like β″ phase is considered to be the main strengthening phase in peak aging. It has a C-centered monoclinic structure with lattice parameters $a$ = 1.516 nm, $b$ = 0.405 nm, $c$ = 0.674 nm and β = 105.3°. The chemical composition of β″ is identified as $Mg_5Al_2Si_4$ [4, 11, 12]. Close-ups of the cross-section show that β″ is essentially a stack of identical units with an eye-like appearance

which consist of nine atomic columns with 4-fold symmetry. This structural unit was referred to as a "low density cylinder" (LDC) in previous research [13]. The β′ phase formed during over aging has a stoichiometry of $Mg_9Si_5$, a space group of hexagonal $P6_3/m$, and the lattice parameters of $a$ = 0.715 nm and $c$ = 0.405 nm [6, 14]. The U1, U2 and B′ are also labelled as type A, type B and type C, respectively [7, 15, 16]. The β phase and Si particle are formed at the equilibrium stage.

Addition of Cu or Ag is known to be effective in increasing the precipitation strengthening for Al-Mg-Si alloys [17-20]. Cu suppresses the precipitation of β″ phase and facilitates the formation of Cu-containing phases, such as Q′, QP1, QP2, C and Q, thus changes the precipitation sequence of Al-Mg-Si alloys [21-26]. Compared with Cu, Ag could not only significantly improve the aging hardening response and hardening kinetics for Al-Mg-Si alloys during artificial aging, but also guarantee a relatively low strength in T4 temper, which provides a good balance between formability and bake hardening potential [17, 27-30]. At the early aging stage, Ag facilitates the formation of clusters for Al-Mg-Si alloys. High density of clusters lead to a finer and denser distribution of β″ phase and thus improves the peak hardness for these alloys [31]. C.D. Marioara et al. [32] investigated the atomic structure of β′ phase in an over-aged Al-Mg-Si-Ag alloy by high angle annular dark field scanning transmission electron microscopy (HAADF-STEM). They found that Ag can enter β′ phase and replace certain Si atomic columns, changing the space group from $P6_3/m$ (β′) to P62m ($β'_{Ag}$) and the composition from $Mg_9Si_5$ (β′) to $Al_3Mg_3Si_2Ag$ ($β'_{Ag}$). K. Matsuda et al. [33] reported a new grain boundary precipitate (GBP) in the over-aged Al-Mg-Si-Ag alloy. This precipitate is a quaternary MgSiAgAl phase with a hexagonal crystal structure and the ratio of Mg:Si:Ag in this new GBP phase is 8:5:2 or 9:5:2. The quaternary GBP has a lattice parameter larger than that of Q′ phase in Al-Mg-Si-Cu alloys. E. A. Mørtsell [34] and T. Saito [30] et al. investigated the $Q'_{Ag}$ phase in an Al-Mg-Si-Ag alloy, its composition is identified as $Mg_9Si_7Ag_2Al_3$ and the lattice parameters are $a = b$ = 1.032 nm, $c$ = 0.405 nm, γ = 120°. Although the influence of Ag on the precipitation of Al-Mg-Si alloys has been investigated by different researchers, most of these works focus on one single precipitate (such as β′ phase) in a given aging condition. The influence of Ag on the whole precipitation sequence of Al-Mg-Si alloys has not been systematically investigated which opens some fundamental questions as follow, (1) The effect of Ag on the atomic structures of GP zone and β″ phase formed at the early and peak aging stage is largely unknown, (2) The formation mechanisms of $β'_{Ag}$ and $Q'_{Ag}$ phases formed at over aging are not fully understood, (3) The role of Ag on the structural evolution of various precipitates in the Al-Mg-Si-Ag alloy during artificial aging is not clear. Understanding the mechanism of Ag influence on the precipitation of Al-Mg-Si alloys is essential for

improving the properties of these alloys.

Ag, as a main microalloying element in aluminum alloy, could not only substantially enhance the precipitation by altering the structure of precipitates, but is also prone to segregate at the interfaces of different precipitates. J.M. Rosalie et al. [35] reported that Ag atoms strongly segregate to the coherent, planar interface of θ′ phase in the Al-Cu-Ag alloy. S.J. Kang et al. [36] revealed that the Ag and Mg co-segregation at the $\{111\}_{\alpha}$ habit plane of Ω phase plays a decisive role in the excellent thermal stability of the Al-Cu-Mg-Ag alloys at temperature up to 200 °C. C.D. Marioara et al. [32] reported the segregation of Ag atoms at the β′/α-Al interface of Al-Mg-Si-Ag alloy, and found that in most case, Ag atoms replace the Al atoms in the FCC matrix. It is generally argued that segregation of solute atoms at the precipitate/matrix interface has a significant impact on the morphology and strengthening ability of precipitate, and thus influences the mechanical property of alloys. Therefore, understanding the Ag segregation at the precipitate/matrix interface is extremely important for the properties improvement. Till now, the underlying segregation mechanism of Ag atoms at the precipitate/matrix interface is not clear, and the influence of Ag segregation on the precipitation evolution of Al-Mg-Si alloy is still not understood.

In the present work, atomic-resolution HAADF-STEM, atom probe tomography (APT) combined with density functional theory (DFT) calculation were performed to investigate the effect of Ag addition on the precipitation evolution for Al-Mg-Si alloys. The mechanism of Ag influence on the atomic structure of precipitates was explored. The segregation mechanism of Ag at the precipitate/α-Al matrix interface and the influence of Ag segregation on the precipitate morphology evolution and mechanical property for the Al-Mg-Si-Ag alloy were systematically investigated and discussed.

## 2. Experimental

The chemical compositions of the two investigated Al-Mg-Si alloys are listed in Table 1. The two alloys have the same Mg and Si contents but different Ag addition, the A1 alloy is the base alloy without Ag addition and the A2 alloy has 0.49 wt. % Ag addition. The Mg/Si ratios of the two alloys are 1.77 and 1.85, respectively, which correspond to a Mg-rich alloy. Fe and Mn as impurity are present in two alloys. The as-cast alloys were homogenized at 560 °C for 6h, and cold rolled to 1 mm thick sheets after hot rolling. These sheets were then solution heat treated at 570 °C for 20 min and water quenched to room temperature, followed by immediately artificial aging (AA) at 170 °C for different times.

Table 1 Chemical compositions of the two investigated alloys

| Alloy | | Mg | Si | Fe | Mn | Ag |
|---|---|---|---|---|---|---|
| A1 | wt.% | 1.09 | 0.71 | 0.11 | 0.06 | - |
| | at.% | 1.21 | 0.68 | 0.05 | 0.03 | - |
| A2 | wt.% | 1.13 | 0.71 | 0.11 | 0.06 | 0.49 |
| | at.% | 1.26 | 0.68 | 0.05 | 0.03 | 0.12 |

Vickers microhardness was measured after AA treatment using a MH-5L microhardness tester with a load of 500 g and a dwell time of 10s. The microstructures of the two alloys in different AA condition were investigated by FEI Tecnai G2 F20 TEM. For each alloy condition, at least twenty TEM bright-field images were taken to compare and make statistical comparisons. Atomic resolution HAADF-STEM characterization was performed using a spherical aberration probe corrected FEI Titan G2 60-300 ChemiSTEM with a Schottky field emitter operated at 300 kV. The probe diameter was 0.08 nm, and a 21 mrad convergence semi-angle and a spot size 7 were used for HAADF imaging and EDS data collection in STEM mode. All TEM images were taken along the $<001>_{\alpha}$ zone axis to characterize the cross-sections of needle/rod/lath precipitates. All HAADF-STEM images were Fourier filtered with an aperture encompassing all the visible spots in the Fourier transform. Disc-shaped TEM specimens were prepared by electro polishing using a Struers TenuPol-5 machine with an electrolyte of 1/3 $HNO_3$ in methanol at a temperature about -30 $^{o}$C. The APT analysis was obtained on a CAMECA LEAP4000HR instrument with a voltage pulse repetition rate of 200 kHz, a voltage pulse fraction of 20% and a detector efficiency of 36%. The analysis of the APT data was carried out using IVAS$^{TM}$ 3.6.8 software. The 5th nearest-neighbour (5NN) distance distributions of solute atoms were used to evaluate the overall extent of clustering by creating frequency histograms of the datasets. A maximum distance between atoms ($d_{max}$) of 0.5 nm and a minimum number of solute atoms ($N_{min}$) of 10 solute atoms were used.

DFT calculation employed Vanderbilt ultrasoft pseudopotentials as implemented in the plane wave (PW) based code Vienna Ab initio Simulation Package (VASP). The Perdew-Wang generalized gradient approximation was used for the exchange-correlation energy. All calculations of unit cell models were performed with an energy cut-off of 450 eV and a *k*-point grid of 12 × 12 × 12. The formation enthalpy of these models was calculated based on the formula given in the reference [37], which is directly proportional by inversion to the stability of the structure. The formation enthalpy of the $\Delta H_{ss}$ ($Al_aMg_bSi_c$) and $\Delta H_{ss}$

($Al_xMg_ySi_zAg_k$) are defined with respect to the enthalpies of the constituent elements in solid solution.

$$\Delta H_{ss}(Al_aMg_bSi_c) = H(Al_xMg_ySi_z) - aH(Al_{fcc}) - bH(Mg_{sub}) - cH(Si_{sub})$$

$$\Delta H_{ss}(Al_xMg_ySi_zAg_k) = H(Al_xMg_ySi_zAg_k) - xH(Al_{fcc}) - yH(Mg_{sub}) - zH(Si_{sub}) - kH(Ag_{sub})$$

Where a, b, c and x, y, z, k are the atomic fractions (a + b + c = 1) and (x + y + z + k = 1). The $H(Mg_{sub})$, $H(Si_{sub})$ and $H(Ag_{sub})$ are the enthalpies of the Mg, Si and Cu atoms on substitutional sites in the Al matrix. The enthalpy $H(Mg_{sub})$ is calculated by employing 3 × 3 × 3 fcc Al supercells consisting of 108 atoms with a k-mesh of 11 × 11 × 11.

$$H(Mg_{sub}) = H(Al_{107}Mg) - 107/108H(Al_{108})$$

An analogous formula is valid for $H(Si_{sub})$ and $H(Ag_{sub})$.

For the calculation of the formation energy of precipitate interfaces with and without Ag additions, the energy of Ag in solution is also included in the calculation. We used the generalised gradient approximation of Perdew, Burke, and Ernzerhof (GGA-PBE) [38] using the projector augmented wave (PAW) method [39, 40] implemented in VASP [41]. Geometrical relaxations were performed to optimise the supercells until Hellmann-Feynman forces were less than 0.01 eV/Å, using the Methfessel-Paxton method [42] with a smearing factor of 0.05 eV. All lattice parameters and all internal coordinates were optimised. Single-point energy calculations were performed using the tetrahedron method with Blochl corrections [43]. The Brillouin zone was sampled using the Gamma-centred k-point grids, which is particularly efficient for hexagonal lattices. The convergence of the relevant energy differences with respect to energy cut-off (500 eV), k-point sampling (~6000/atom) and supercell size was better than 1 meV/atom. All the calculations were performed following the structure optimisation and static energy calculation workflow implemented in Atomate [44]. The Ag interfacial segregation energy is defined as the formation energy difference per Ag atom for interfacial structures with and without Ag segregation with a reference of Ag energy in solid solution.

$$\Delta H_{ss}(Al_aMg_bSi_c\text{-}Al_{\ interface}) = \Delta H_{ss}(Al_xMg_ySi_zAg_k)/k - H(Ag_{sub})$$

# 3. Results

## 3.1. Hardness measurements

Fig. 1 shows the hardness curves of the two investigated alloys aged at 170 ºC for different times immediately after water quenching. The hardness evolution of these two alloys is similar, i.e. the hardness increased rapidly to a maximum and decreased slowly with increasing aging time. Compared with the A1 base alloy, the Ag-added A2 alloy presented an overall higher hardness and shorter time to reach the peak hardness. It is obvious that Ag addition could enhance the precipitation hardening and precipitation kinetics for Al-Mg-Si alloys.

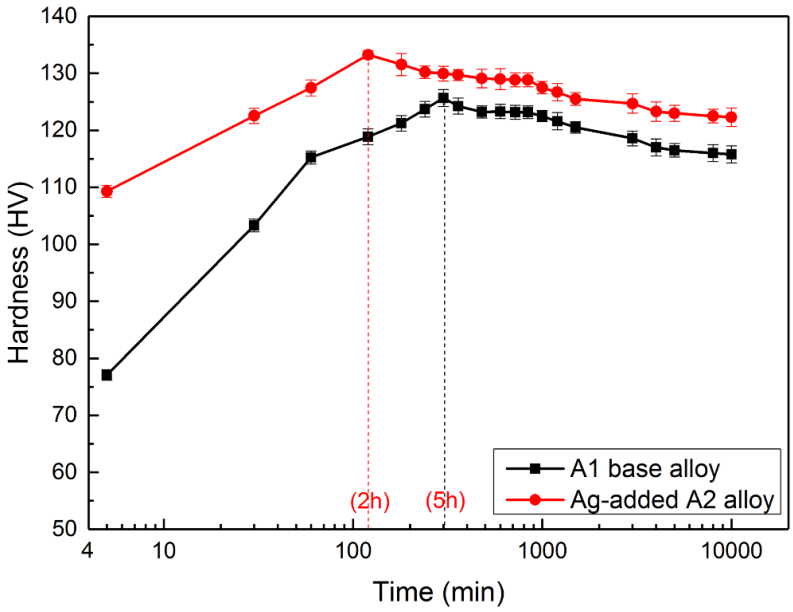


Fig. 1. Evolution of Vickers hardness for the two investigated alloys during AA at 170 ºC immediately after water quenching.

## 3.2. TEM characterization

TEM characterization was performed to reveal the influence of Ag addition on microstructure for Al-Mg-Si alloys. Fig. 2 shows representative TEM bright-field micrographs of precipitates formed in the two alloys during AA at 170 ºC for different times (2h, 5h, 2 days, 1 week). For both alloys, the precipitate size was increased while the number density of precipitate was decreased. Based on the HAADF-STEM images and corresponding Fast Fourier transforms (FFT) patterns shown in Fig. 3, the needle-like and rod-like precipitates formed in A1 alloy under peak aging and over aging conditions were identified as β″ and β′ phases, respectively. The Ag-added A2 alloy had the same type of precipitates as A1 alloy, and the detailed atomic structures of these precipitates will be presented in the next section. The quantification of precipitates for the two alloys determined from the TEM bright-field images of Fig. 2 is listed in Table 2, and the

precipitate length distributions are presented in Fig. 4. It could be found that the number density and volume fraction of precipitate in the Ag-added A2 alloy were higher than that of the A1 base alloy both at peak-aged and over-aged stages, implying that Ag addition could promote the formation of precipitates and refine their distribution. The length/diameter ratios of β″ precipitate in both alloys were quite similar at the peak-aged stage. While at the over-aged stage, the β′ precipitate in the A2 alloy had significantly larger length/diameter ratio than that of the A1 alloy, which means that Ag addition could change the morphology of β′ precipitate from stubby to slender after long-time aging.

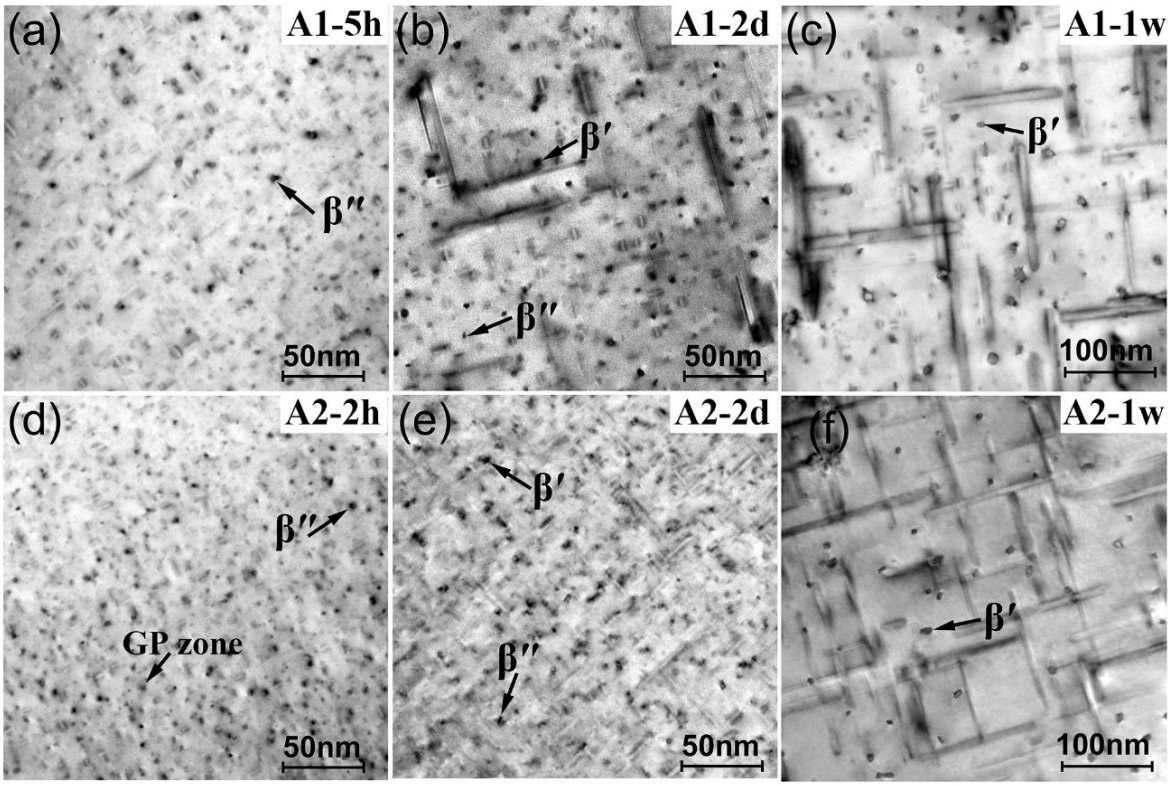


Fig. 2. TEM bright-field images of the two alloys aged at 170 °C for different times. (a) A1, 5h peak aging, (b) A1, 2 days AA, (c) A1, 1 week AA, (d) A2, 2h peak aging, (e) A2, 2 days AA, (f) A2, 1 week AA.

Table 2 Statistics of β″ and β′ precipitates for the two alloys after AA at different aging times.

| | AA | | Average length (L, nm) | Cross-section ($nm^2$) | Length/Diameter ratio | Number density [$\mu m^{-3}\times$ (1000)] | Volume fraction (%) |
|---|---|---|---|---|---|---|---|
| β″ | Peak aging-5h | A1 | 8.45±1 | 13.58±0.2 | 4.06 | 21.20±0.2 | 0.24±0.02 |
| β″ | Peak aging-2h | A2 | 6.25±1 | 9.25±0.3 | 3.64 | 55.30±0.2 | 0.32±0.02 |
| β′ | Over aging-1w | A1 | 65.92±2 | 19.85±0.4 | 13.11 | 4.19±0.2 | 0.55±0.06 |
| β′ | | A2 | 109.46±3 | 15.7±0.3 | 24.49 | 4.94±0.3 | 0.85±0.07 |

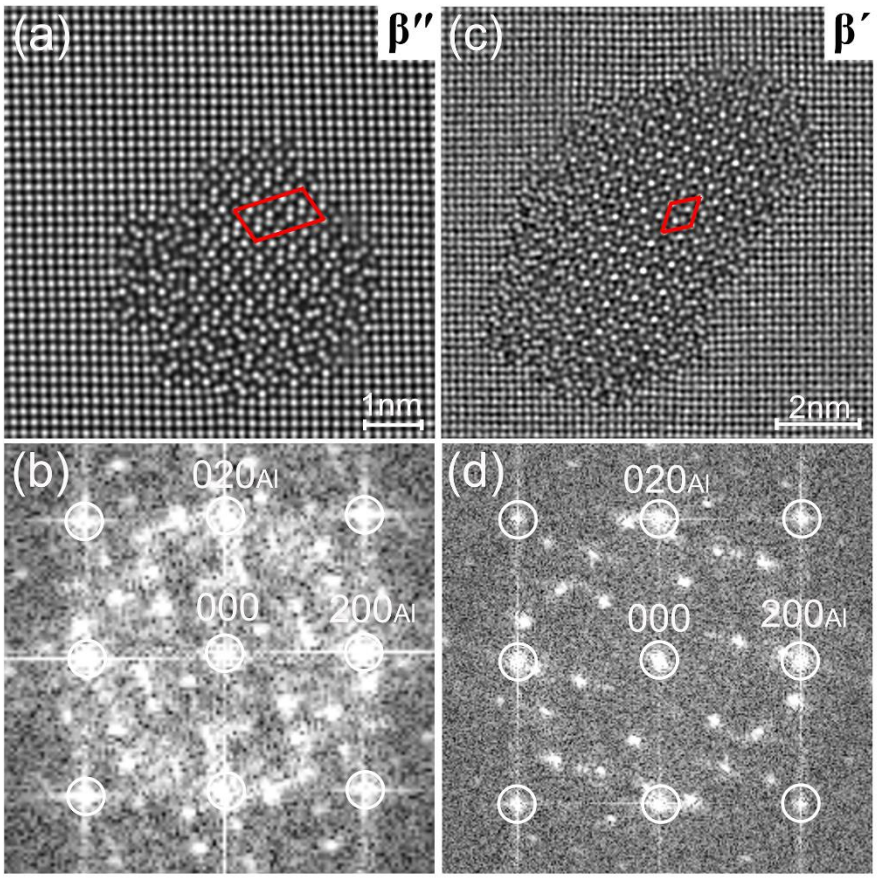


Fig. 3. (a) HAADF-STEM image of β″ precipitate formed at 5h peak aging for the A1 base alloy, (c) HAADF-STEM image of β′ precipitate formed at one week over aging for the A1 base alloy. (b, d) corresponding FFT patterns of (a, c), respectively. The unit cells of β″ and β′ are marked by red lines.

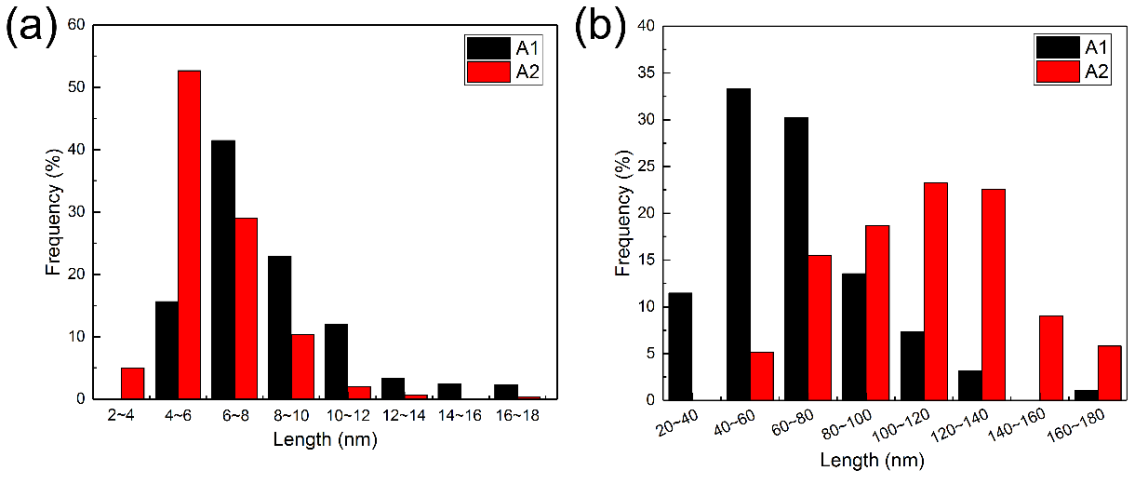


Fig. 4. Precipitate length distribution of β″ and β′ precipitates for the two alloys, (a) β″, peak aging, (b) β′, one week AA.

## 3.3. APT and HAADF-STEM characterizations for the Ag-added A2 alloy

### 3.3.1. early-aged microstructure

At the early stage of aging, atomic clusters are formed and responsible for the strengthening of these alloys. The distribution of Ag atoms in clusters of the Ag-added A2 alloy was investigated by APT technique. Fig. 5 (a) shows APT elemental maps of solute atoms in the A2 alloy aging at 170 ºC for 5 min. The Mg, Si and Ag atoms are depicted as purple, blue and red spheres, respectively. In order to clearly elucidate the clusters, the Al atom is not displayed in the elemental maps. An enlarged APT map of the clusters is presented in Fig. 5 (b), it could be clearly seen that a large number of clusters were formed in the A2 alloy and Ag atoms incorporated into the clusters. Fig. 5 (c) shows the frequency histograms of Mg, Si and Ag atoms obtained from both experimental and randomized data based on 5NN distances. It could be seen that for the Mg, Si and Ag atoms, the experimental histograms broaden in comparison to their respective random curves, shifting to smaller NN distances, which serves as evidence for solute clustering as distinct from a random configuration of solute atoms within the solid solution. The Ag/Mg ratio as a function of the cluster size is plotted in Fig. 5 (d). Variation of the Ag/Mg ratio in clusters becomes narrower with increasing the cluster size, implying that the clusters with size larger than 1nm are prone to have a constant Ag/Mg ratio.

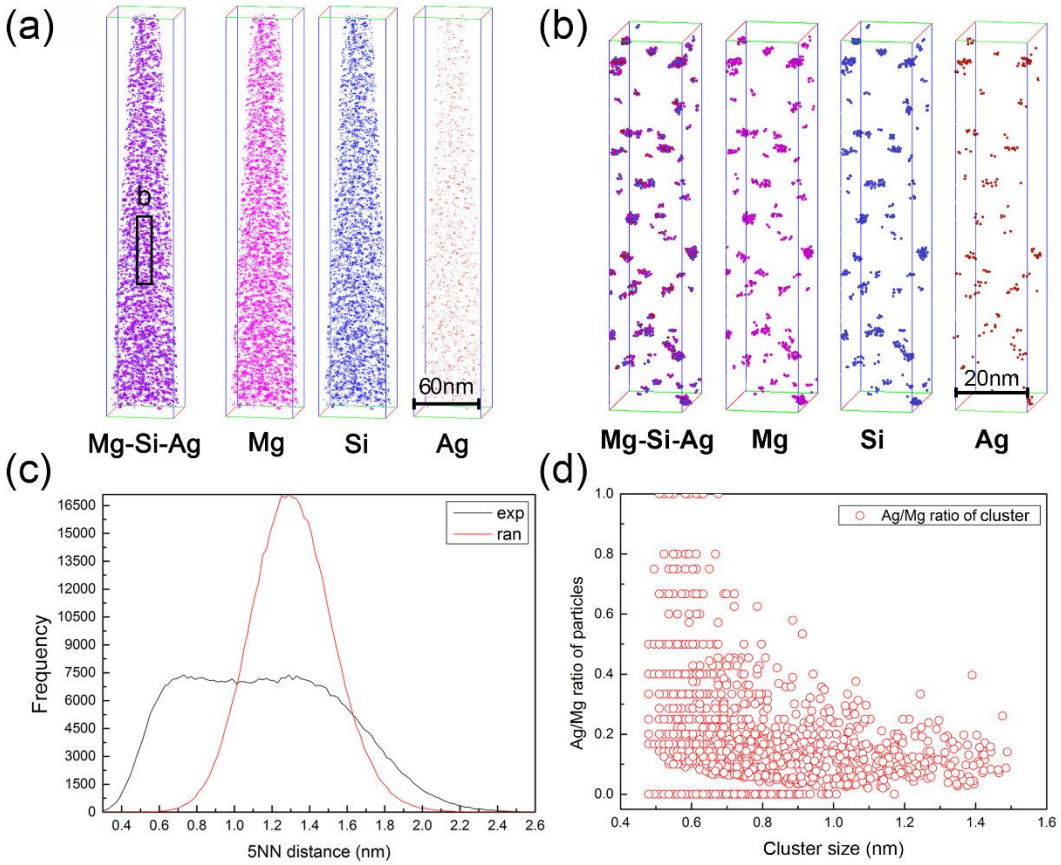


Fig. 5. (a) Atoms maps for the Ag-added A2 alloy after AA at 170 ºC for 5 min, (b) the enlarged 3DAP maps of the zone b marked in (a), (c) frequency histograms (experimental in black and randomly labelled in red) of 5NN distance between Mg, Si and Cu solute atoms, (d) the measured Ag/Mg ratio plotted against the cluster size.

## 3.3.2 Peak-aged microstructure

HAADF-STEM images and the corresponding FFT patterns of the GP zone and β″ phase formed in the peak-aged A2 alloy are shown in Fig. 6. Due to the intensity of HAADF-STEM images varying approximately as the square of atomic number, $Z^2$, Ag column could be easily identified for its strong atomic number relative to other elements (Z = 47 for Ag, Z = 13 for Al, Z = 12 for Mg, Z = 14 for Si). It could be seen that the GP zone still maintained the FCC structure with some local ordered region marked by the dashed red circle, similar to the substructure of β″- "low density cylinder (LDC)" [13]. Ag atoms were found to segregate at the GP zone/α-Al interface by the replacement of Al atom in FCC matrix, and no Ag atom was found in the interior of GP zone. This phenomenon is different from the Cu addition, in which Cu could

incorporate into the interior of GP-zone and form its local symmetry, Cu sub-unit cluster, in Al-Mg-Si-Cu alloys [26]. More images of GP zones formed in the peak-aged A2 alloy are presented in Supplementary Fig. S1. For the β″ precipitates shown in Figs. 6 (b-d), the β″ unit cell and its substructure LDC were clearly observed. The orientation relationship (OR) between β″ phase and the α-Al matrix can be identified as: $[010]_{\beta''}$ // $[001]_{\alpha}$, $(100)_{\beta''}$ // $(320)_{\alpha}$, and $(001)_{\beta''}$ // $(\bar{1}30)_{\alpha}$, which corresponds well to the previous literature [8, 45, 46]. Except for β″ unit cell, the U2 and β′ unit cells co-existed in some precipitates, as seen in Fig. 6 (c and d). The OR between β″, U2, β′ unit cells and α-Al can be identified as $[001]_{\beta''}$ // $[100]_{U2}$ // $[100]_{\beta'}$ // $[\bar{1}30]_{\alpha}$ and $[010]_{\beta''}$ // $[010]_{U2}$ // $[001]_{\beta'}$ // $[001]_{\alpha}$. For all the observed β″ precipitates in the A2 alloy, Ag segregation was found at the β″/α-Al interface by the replacement of Al site in FCC matrix, and the segregation of Ag atoms seems to favor the $(100)_{\beta''}$ plane. At this aging stage, nearly no Ag atom was observed in the interior of β″ precipitates.

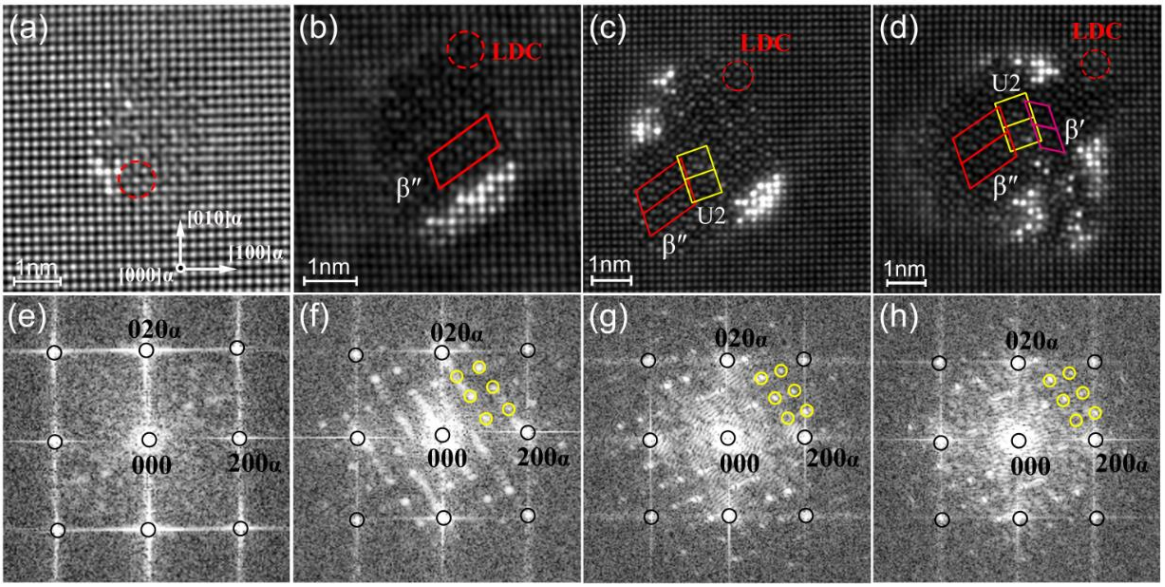


Fig. 6. (a, b, c, d) HAADF-STEM images of GP zone and β″ phases formed in the peak-aged condition (170 $^{o}$C for 2h) for the Ag-added A2 alloy, (a) GP zone, (b, c, d) β″ phase. (e, f, g, h) the corresponding FFT patterns of (a, b, c, d), respectively. The β″, U2 and β′ cell units are marked by the red, yellow and purple lines, respectively. The low density cylinder (LDC) is marked by the dashed red circle.

## 3.3.3. Over-aged microstructure

Figs. 7 (a, b) show the HAADF-STEM image and the corresponding FFT pattern of the β″ phase formed in the Ag-added A2 alloy after 2 days over-aging. At this aging stage, it was clear that Ag atoms gradually

incorporate into the interior of β″ phase. In the Ag-containing region, the β″ unit cell was disappeared and the QP lattice (a hexagonal network of Si atomic columns [26], termed as "Si network" by previous researcher [21]) was formed as marked by green lines in Figs. 7 (c, g), indicated that Ag incorporation could distort the β″ unit cell and facilitate the formation of QP lattice. Figs. 7 (e and f) show the HAADF-STEM image and the corresponding FFT pattern of the $Q'_{Ag}$ phase formed at the same aging stage. The $Q'_{Ag}$ phase was found to have the same structure as the Q′ phase formed in Al-Mg-Si-Cu alloys, except for the Cu atoms were replaced by the Ag atoms. The hexagonal lattice parameters of the $Q'_{Ag}$ phase were measured as $a = b = 1.032$ nm, $c = 0.405$ nm and $\gamma = 120^{o}$, which is in agreement with a previous report [30]. For both of the Ag-containing β″ and the $Q'_{Ag}$ phase, it could be seen that a common QP lattice was visible in the Ag-containing region as indicated by the green line in Figs. 7 (c and g). Normally, the Ag atom occupied two different positions: the Si site in QP lattice and the site in-between QP lattice. For Ag replacing the Si site in QP lattice, a triangular sub-unit cluster composed of Mg and Al atoms distributed around an Ag atom was formed [32], this substructure is named as Ag-subunit (1) in the present work. When Ag replacing the site in-between QP lattice, a configuration that three Si and three Mg surrounding an Ag atom was formed, which is named as Ag-subunit (2). The arrangement of atoms in Ag-subunit (2) is similar to the Cu sub-unit cluster observed in Cu-containing precipitates (i.e. Q′ and C ) for Al-Mg-Si-Cu alloys [26], except for the Cu atom is replaced by Ag atom. The Ag-subunit (2) was also named as the Q′/C-local configuration by E.A. Mørtsell et al. [34], is the stable structure of the $Q'_{Ag}$ unit cell. These results suggest that Ag atoms could enter β″ phase and form their own symmetry structures, Ag-subunit (1) and Ag-subunit (2). Besides, a large number of Ag atoms were segregated at the β″/α-Al interface by occupying the Al site in FCC matrix.

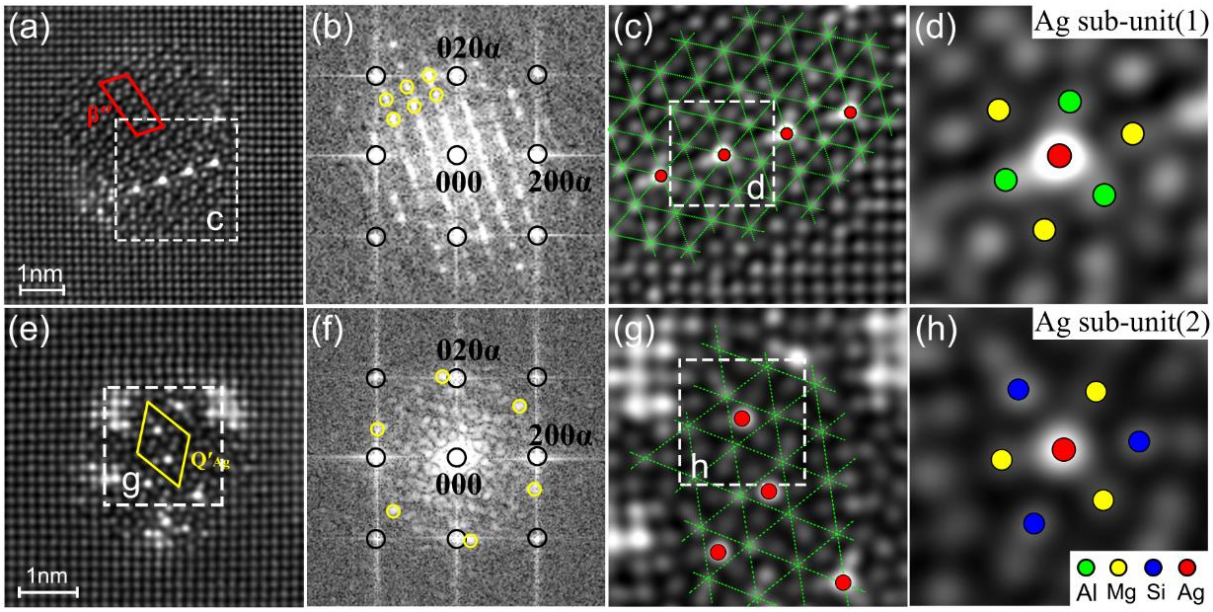


Fig. 7. (a, e) HAADF-STEM images of β″ and $Q'_{Ag}$ phases formed at the over-aged condition (170 °C for 2 d) for the Ag-added A2 alloy. (b, f) the corresponding FFT patterns of (a, e), respectively. (c, g) the enlarged HAADF-STEM images of the zone c and g marked in (a and e), respectively. The QP lattice is marked by dashed green lines. (d, h) the enlarged HAADF-STEM images of the zone d and h marked in (c, g), respectively. The β″ and $Q'_{Ag}$ unit cells are marked by the red and yellow lines, respectively.

Fig. 8 shows the HAADF-STEM images and the corresponding FFT patterns of four precipitates formed in the Ag-added A2 alloy after AA for one week. The precipitates presented in Figs. 8 (a and b) could be identified as β′ phase, Ag atoms were found to segregate at the β′/α-Al interface, and only minor Ag atoms were incorporated in the interior of β′ phase as indicated in Fig. 8 (a). In contrast, for the precipitates presented in Figs. 8 (c and d), the precipitates could also be identified as β′ phase from the FFT pattern presented in Fig. 8 (g and h) and Ag segregation were found at the interface. However, a large number of Ag atoms were incorporated into the interior of β′ phase and formed the $\beta'_{Ag}$ unit cell within the precipitate, thus the β′ and $\beta'_{Ag}$ unit cell coexisted within one single precipitate. The $\beta'_{Ag}$ unit cell is isostructural with the β′ unit cell, and thus fully coherent with each other within the precipitate [32]. From the FFT patterns of these precipitates, significant variation of ORs between $\beta'_{Ag}$ phase and the α-Al matrix can be observed. The multiple ORs of $\beta'_{Ag}$ precipitate are similar to the β′ phase reported in our previous work [47], implying that Ag addition does not influence the multiple ORs of β′ phase with the α-Al matrix.

HAADF-STEM images of two $\beta'_{Ag}/\beta'$ composite precipitates are shown in Figs. 9 (a and d), it could be seen that the distribution of Ag atoms in the interior of the composite precipitate was rather heterogeneous, leading to a disordered structure of $\beta'_{Ag}/\beta'$ composite precipitate. All the Ag atoms replaced the Si atomic sites in the QP lattice. Two different arrangements of Ag atoms could be identified within the precipitates: the hexagonal Ag-network in Fig. 9 (e) and the rectangle Ag-network in Fig. 9 (f). The totally different Ag-networks indicate that different $\beta'_{Ag}$ unit cells were formed. The two $\beta'_{Ag}$ unit cells were identified as $\beta'_{Ag1}$ and $\beta'_{Ag2}$, as presented in Figs. 9 (h and i). The main difference between these two $\beta'_{Ag}$ unit cells is the different arrangement of Ag sub-unit (1), resulting from Ag replacing different Si sites in the $\beta'$ unit cell. The schematic illustration of the $\beta'$ unit cell is shown in Fig. 9 (g), it could be seen that the $\beta'$ unit cell has two non-equivalent Si sites, Si1 and Si2. The $\beta'_{Ag1}$ unit cell is formed by Ag atoms replacing the Si1 atoms in the $\beta'$ unit cell, similar to the $\beta'_{Ag}$ phase reported by C.D. Marioara et al. [32], which has a space group P-62*m* and a composition $Mg_3Si_2AgAl_3$. The $\beta'_{Ag2}$ unit cell is firstly reported in the present study, which is formed by Ag atoms replacing the Si2 atoms in the $\beta'$ unit cell. An atomic model for the $\beta'_{Ag2}$ can be constructed by taking into consideration of projected atomic column positions and inter-atomic distances. The space group of $\beta'_{Ag2}$ was identified as P-62*m* for its high symmetry, which is the same as $\beta'_{Ag1}$. The hexagonal lattice parameters of the $\beta'_{Ag2}$ unit cell were measured as $a = b = 0.720$ nm, $c = 0.405$ nm, which are slightly larger than those of $\beta'_{Ag1}$ and $\beta'$ unit cells. The composition of $\beta'_{Ag2}$ unit cell was identified as $Mg_3SiAg_2Al_3$ according to the atomic position in the HAADF-STEM image. The precipitates with larger $\beta'_{Ag2}$ regions are shown in Supplementary Fig. S2. The structures of $\beta'$, $\beta'_{Ag1}$ and $\beta'_{Ag2}$ unit cells with the positions (x, y, z) of solute atoms are listed in Table 3. Statistical analyses indicated that most precipitates formed at the over-aged stage have a composite structure: mixed of the $\beta'_{Ag1}$, $\beta'_{Ag2}$, $Q'_{Ag}$ and $\beta'$ unit cells.

Ag segregation was observed at the $\beta'_{Ag}/\alpha$-Al interface in almost all the $\beta'_{Ag}$ precipitates. Fig. 10 shows HAADF-STEM images of the $\beta'_{Ag}$ precipitates formed after AA for one week in the Ag-added A2 alloy. Ag atoms mainly occupied two positions at the interface: the Al atom in the FCC matrix and the Si atom in the $\beta'$ phase as shown in Figs. 10 (b and c), respectively. In addition, Ag atoms preferentially segregated at the $\beta'/\alpha$-Al semi-coherent interface along the $[100]_\alpha$ direction, as shown in Fig. 10 (f). But no Ag segregation was observed at the $\beta'/\alpha$-Al coherent interface shown in Fig. 10 (e).

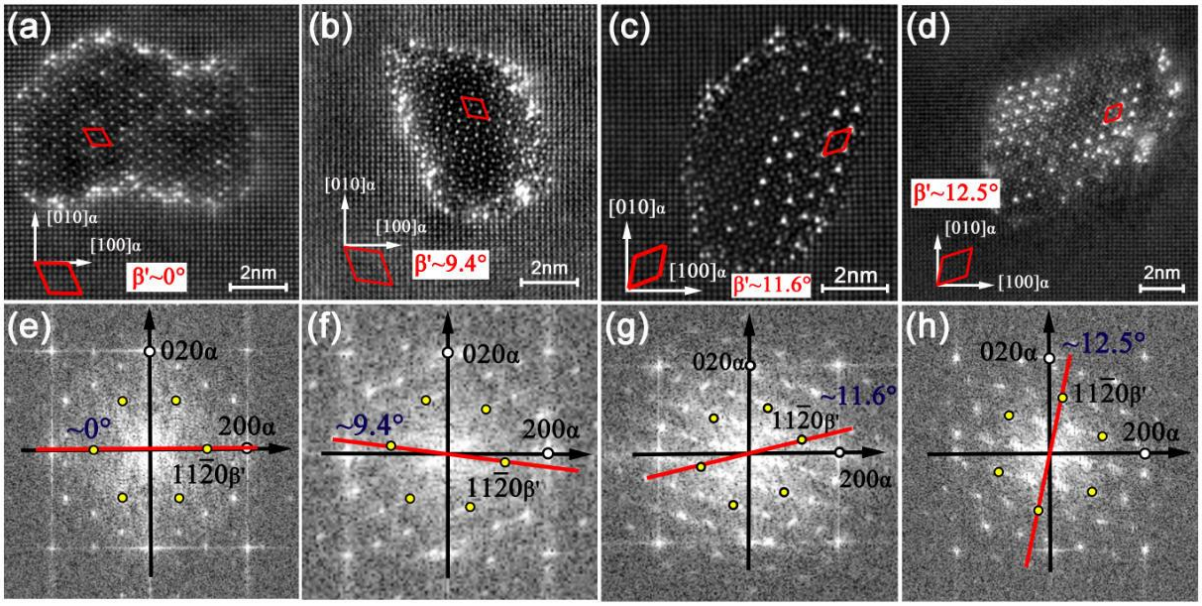


Fig. 8. (a, b, c, d) HAADF-STEM images of four individual $\beta'_{Ag}$ precipitates formed after one week AA for the Ag-added A2 alloy, (e, f, g, h) the corresponding FFT patterns of (a, b, c, d), respectively. The β′ and $\beta'_{Ag}$ unit cells are marked by red lines.

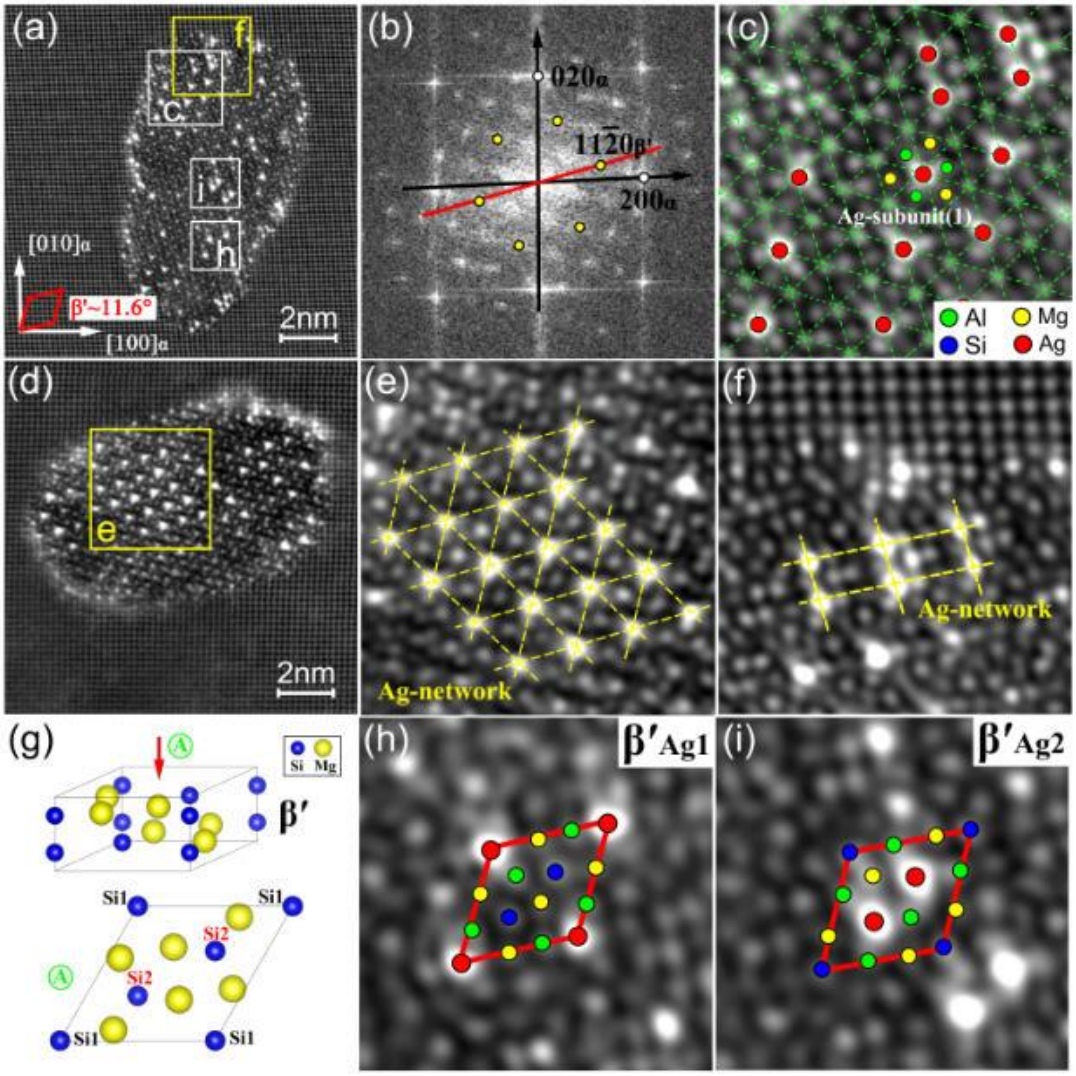


Fig. 9. (a, d) HAADF-STEM images of $\beta'_{Ag}$ precipitates formed at the over-aged condition (170 °C for one week). (b) the corresponding FFT pattern of (a). (c, f, h, i) the enlarged HAADF-STEM images of the zones marked in (a). (e) the enlarged HAADF-STEM image of the zone marked in (d). (g) schematic illustration of the β′ unit cell. The $\beta'_{Ag}$ cell unit is marked by the red lines. The QP lattice and Ag-network are marked by dashed green and yellow lines, respectively.

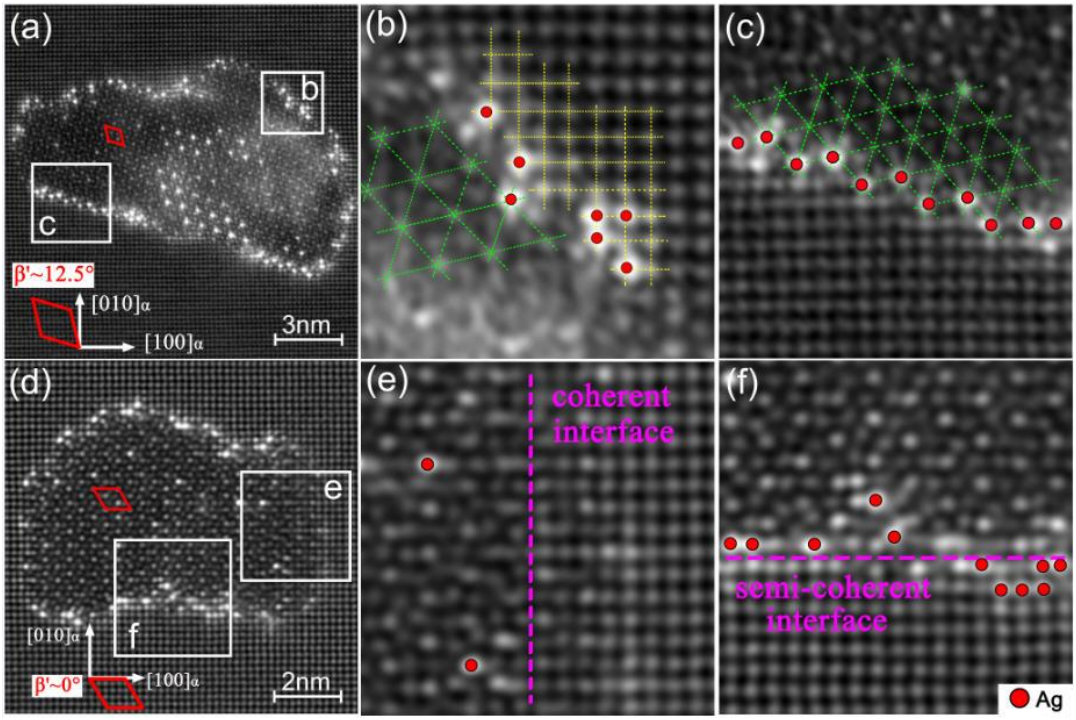


Fig. 10. (a, d) HAADF-STEM images of $\beta'_{Ag}$ precipitates formed at the over-aged condition (170 °C for one week). (b, c) and (e, f) are the enlarged HAADF-STEM images of the zones marked in (a) and (d), respectively. The QP lattice and Al matrix are marked by dashed green and yellow lines, respectively. The β′ cell unit is marked by the red lines.

Table 3 Comparison between the crystal structure of β′, $\beta'_{Ag1}$ and $\beta'_{Ag2}$ unit cells.

| | **β′ [32]** | | | | | **$\beta'_{Ag1}$ [32]** | | | | | **$\beta'_{Ag2}$** | | | | |
|---|---|---|---|---|---|---|---|---|---|---|---|---|---|---|---|
| **Lattice parameters** | $a = b = 0.715$ nm, $c = 0.405$ nm | | | | | $a = b = 0.690$ nm, $c = 0.405$ nm | | | | | $a = b = 0.720$ nm, $c = 0.405$ nm | | | | |
| **Space group** | hexagonal $P6_3/m$ | | | | | hexagonal P-62m | | | | | hexagonal P-62m | | | | |
| **Composition** | $Mg_{1.8}Si$ | | | | | $Mg_3Si_2AgAl_3$ | | | | | $Mg_3SiAg_2Al_3$ | | | | |
| **Atomic position** | **Atom** | **x** | **y** | **z** | **Occ.** | **Atom** | **x** | **y** | **z** | **Occ.** | **Atom** | **x** | **y** | **z** | **Occ.** |
| | **Si1** | 0 | 0 | 0.25 | 2/3 | **Ag** | 0 | 0 | 0 | 1 | **Si** | 0 | 0 | 0 | 1 |
| | **Si2** | 2/3 | 1/3 | 0.25 | 1 | **Si** | 1/3 | 2/3 | 0.5 | 1 | **Ag** | 1/3 | 2/3 | 0.5 | 1 |
| | **Mg** | 0.6153 | 0.6954 | 0.25 | 1 | **Al** | 0.74 | 0.74 | 0.5 | 1 | **Mg** | 0.7375 | 0.7375 | 0.5 | 1 |
| | | | | | | **Mg** | 0.40 | 0.40 | 0 | 1 | **Al** | 0.3825 | 0.3825 | 0 | 1 |

## 3.3.4. Equilibrium microstructure

Fig. 11 (a) shows the low-magnification HAADF-STEM image of microstructure for the Ag-added A2

alloy aged at 300 ºC for two weeks, which is thought to be the equilibrium stage. The plate precipitate is identified as β ($Mg_2Si$) phase by STEM-EDS analysis. Most Ag atoms were presented in the α-Al matrix, and no Ag atoms were detected in the interior of β phase, indicating that Ag atoms were released into the α-Al matrix during the long-time over-aging treatment. Besides, few spherical Ag particles were occasionally observed in the α-Al matrix, shown in Figs. 11 (f-j).

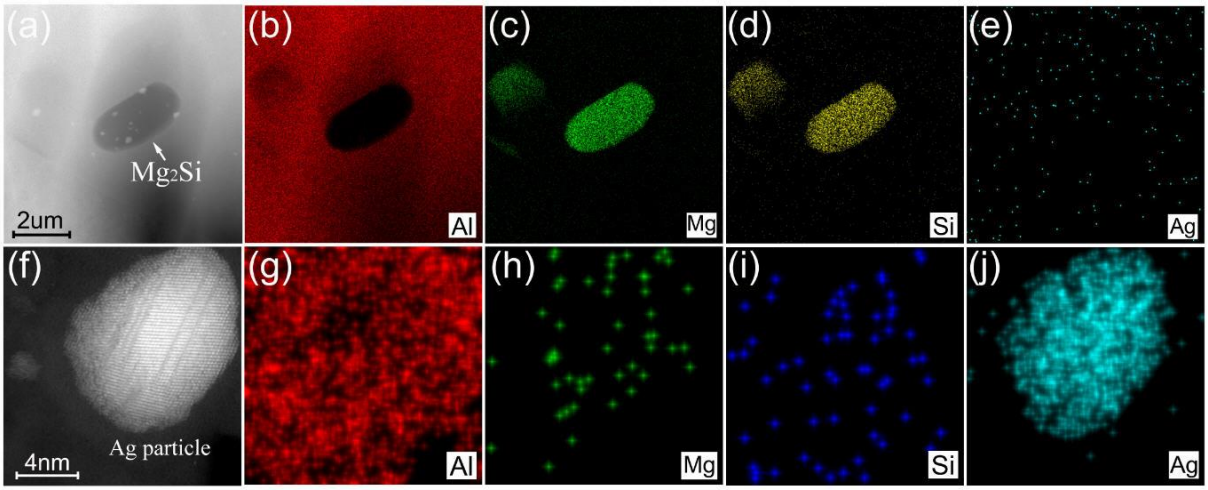


Fig. 11. (a) HAADF-STEM image of the Ag-added A2 alloy at an equilibrium stage (300 ºC AA for two weeks). (b-e) STEM-EDS maps of (a), (f) HAADF-STEM image of Ag particle, (g-j) STEM-EDS maps of (f).

# 4. Discussion

## 4.1. Influence of Ag on the structural evolution of precipitates in Al-Mg-Si alloy

For Al-Mg-Si alloys, Ag addition could change the atomic structure, morphology and distribution of precipitates during aging treatment, which significantly affects the mechanical properties of these alloys. To reveal the influence mechanism of Ag on the atomic structure of precipitates for Al-Mg-Si alloys, systematic DFT calculations of the precipitates with and without Ag incorporation were performed. The formation enthalpies (ΔH) of various Ag-containing metastable phases are shown in Fig. 12, the ΔH of β″, β′ and β phases are also presented for comparison. The $Mg_{10}Si_8Ag_4$, $Mg_8Ag_2Si_8Al_4$, $Mg_6Ag_4Si_8Al_4$ and $Mg_{10}Ag_4Si_4Al_4$ are built by Ag replacing different Mg or Si sites in the β″ unit cell. From the black line in Fig. 12, it is clear that all the Ag-containing β″ unit cells have higher ΔH than that of the β″ unit cell, indicating

the incorporation of Ag in the β″ unit cell is energetically unfavorable. This well explains why no Ag atom was found in the interior of β″ unit cell. From the red line in Fig. 12, the two $\beta'_{Ag}$ unit cells, $\beta'_{Ag1}$ ($Mg_3Al_3Si_2Ag$) and $\beta'_{Ag2}$ ($Mg_3Al_3SiAg_2$), have the lower ΔH than that of the β′ unit cell, implying that the formation of $\beta'_{Ag1}$ and $\beta'_{Ag2}$ are energetically favorable. For the equilibrium β phase, the two Ag-containing β unit cells ($Ag_2Si$, $Mg_2Ag$) have higher ΔH than that of the β unit cell. This is corresponding very well with the experimental results that no Ag atom was detected in the β phase.

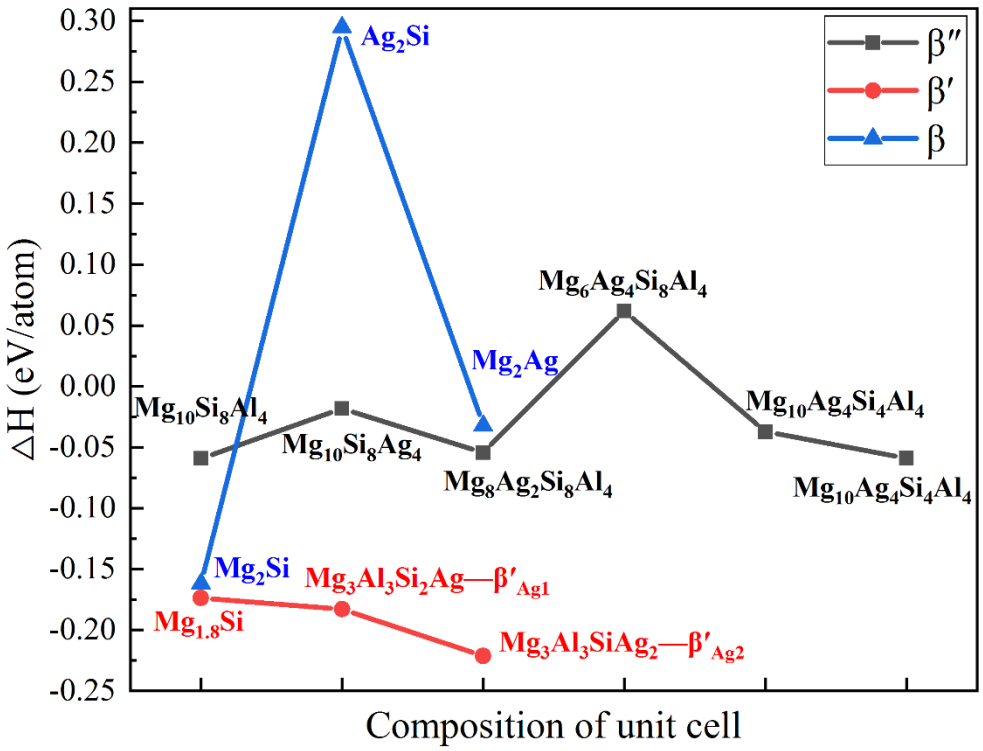


Fig. 12. Formation enthalpy ΔH (eV/atom) plotted as a function of composition, calculated using VASP-PW-GGA.

At the early aging stage, Ag atoms could enter the Mg-Si co-clusters and refine the distribution of clusters by promoting the nucleation of these clusters [29, 31]. As the Ag atoms have a strong interaction energy with the Mg atoms, and high diffusion rate in the matrix, the Ag atoms can incorporate into the Mg-Si co-clusters and "steal" some Mg atoms from the Mg-Si co-clusters to form the Ag-rich clusters and thus refine these clusters. The Ag atoms actually act as the "dispersant", which increases the number density of clusters and precipitates during the early stage of aging. During the following aging process, the Ag addition could change the atomic structure of the precipitates and refine their distribution. At the peak-aged stage, Ag

atoms generally segregate at the GP zone/α-Al and β″/α-Al interfaces by the replacement of Al atom in FCC matrix, and nearly no Ag atom is observed in the interior of GP zone and β″ phase (as shown in Fig. 6). With prolonged aging time, Ag atoms gradually incorporate into the interior of β″ phase, distort the unit cell of β″ and promote the formation of QP lattice (as shown in Fig. 7), and then the two substructures: Ag sub-unit (1) and Ag sub-unit (2) are formed. The Ag sub-unit (1), three Al atoms and three Mg atoms surrounding an Ag atom, is formed by Ag replacing the Si site in QP lattice. The Ag sub-unit (2), three Mg atoms and three Si atoms surrounding an Ag atom, is formed by Ag occupying the site in-between QP lattice. DFT calculations were performed to reveal the structural stability of these two substructures. Fig. 13 display the contour maps of the electron densities of Ag sub-unit (1) and Ag sub-unit (2). A strong covalent bonding is formed between the Ag and Al atoms in the Ag sub-unit (1) as marked by the dashed red circles in Figs. 13 (a and b). But for the Ag sub-unit (2), a strong covalent bonding is observed between the Ag and Si atoms. The strong covalent bondings between Ag and Al/Si atoms play a significant role in stabilizing the substructures of Ag sub-unit (1) and Ag sub-unit (2).

In the over-aging stage, the rearrangement of these substructures results in the formation of $\beta'_{Ag}$ and $Q'_{Ag}$ unit cells within the precipitates. The Ag sub-unit (1) transforms to the $\beta'_{Ag1}$ and $\beta'_{Ag2}$ unit cells and the Ag sub-unit (2) evolves to the $Q'_{Ag}$ unit cell. In the region without Ag, the β″ unit cell could directly transform to the β′ unit cell. The $\beta'_{Ag1}$ and $\beta'_{Ag2}$ unit cells could be distinguished from each other by the different arrangement of Ag sub-unit (1), which is caused by Ag atoms replacing two non-equivalent Si atoms in the β′ unit cell. The $Q'_{Ag}$ phase has the same structure as the Q′ phase formed in the Al-Mg-Si-Cu alloys, except for the Cu atoms are replaced by Ag atoms. During the whole over-aged stage, almost all precipitates have a composite and disordered structure due to the coexistence of different unit cells ($\beta'_{Ag1}$, $\beta'_{Ag2}$, $Q'_{Ag}$ and β′) and the non-periodic arrangement of Ag atoms within the precipitate. This is probably because the diffusion of Ag sub-unit (1) and Ag sub-unit (2) within the precipitate is rather difficult. The sluggish diffusion of these Ag sub-units could lead to a disordered and composite structure of the precipitates. At the equilibrium stage, no Ag atom is detected in the β precipitate and a few Ag particles are observed, meaning that all the Ag atoms are released into the α-Al matrix during the transformation of metastable composite precipitates to the equilibrium β phase, and Ag solid solutionizing in the matrix or forming the Ag particle. Therefore, it can be deduced that Ag atoms undergo a process of "segregate at the precipitate/matrix interface → incorporate into the interior of precipitate → release into the α-Al matrix" during the precipitation for Al-Mg-Si-Ag alloys. Schematic illustration of the precipitate evolution in the Al-Mg-Si-Ag alloy is presented in Fig.14. The

precipitation sequence of the Mg-rich Al-Mg-Si-Ag alloys can be identified as: SSSS → atomic clusters → β″ → $\beta'_{Ag1}$, $\beta'_{Ag2}$, $Q'_{Ag}$, β′ → β, Ag particle. This precipitation sequence is for the first time revealed by atomic-resolution HAADF-STEM technique.

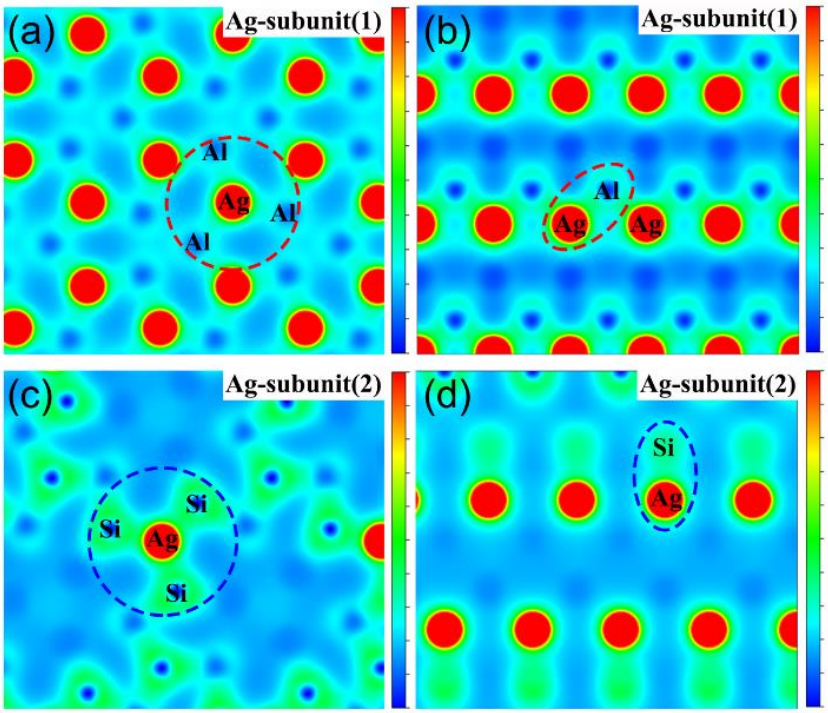


Fig. 13. Contour maps of the electron densities of three phases on different planes calculated using VASP-PW-GGA. (a) $\beta'_{Ag2}$, (001), Z = 0Å, (b) $\beta'_{Ag1}$, (010), Z = 2Å, (c) $Q'_{Ag}$, (001), Z = 0Å, (d) $Q'_{Ag}$, (110), Z = 6Å. The strong covalent bonding between Ag-Al and Ag-Si bonds in $\beta'_{Ag}$ and $Q'_{Ag}$ is displayed by dashed red and blue circles, respectively.

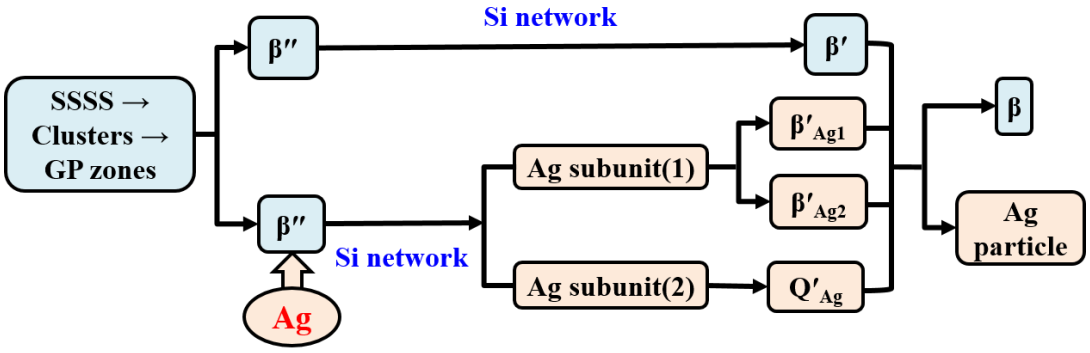


Fig. 14. Schematic illustration of the precipitate evolution in the Mg-rich Al-Mg-Si-Ag alloy.

## 4.2. Ag segregation at the precipitate/matrix interfaces

Ag segregation is found at the interfaces of all metastable phases formed in Al-Mg-Si-Ag alloys, such as the GP zone, β″ and β′ phases. Understanding the interfacial segregation mechanism of Ag atoms is essential to optimize the property of Al-Mg-Si-Ag alloys. Fig. 15 shows the interface structural models of β″/α-Al and β′/α-Al interfaces before and after Ag segregation, which are built based on the HAADF-STEM images shown in Fig. 6 (b) and Fig. 10 (d). The corresponding formation enthalpy △H of these structural-optimized model systems is presented in Fig. 15 (j). It is found that the △H of the β″/α-Al interfaces along the $[\bar{3}10]_{\alpha}$ and $[230]_{\alpha}$ directions and the semi-coherent β′/α-Al interface along the $[2\bar{1}\bar{1}0]_{\beta'}$ direction with Ag segregation are lower than that of these interfaces without Ag segregation. While Ag segregation is not energetically favorable at the coherent β′/α-Al interface along the $[01\bar{1}0]_{\beta'}$ direction. Therefore, Ag preferentially aggregates at the β″/α-Al and semi-coherent β′/α-Al interfaces, but not the coherent β′/α-Al interface, which agrees very well with the experimental results that fewer Ag atoms are found at the coherent β′/α-Al interface (shown in Fig. 10 (e)).

Ag segregation at the interfaces of β″ and β′ phases could change the morphology of precipitates, and thus control the strengthening of Al-Mg-Si alloys. At the over-aged stage, the β′/$\beta'_{Ag}$ composite precipitate in the Ag-added A2 alloy has a higher average length/diameter ratio (L/D = 24.49) than that of the β′ phase (L/D = 13.11) in the A1 base alloy, implying that Ag segregation could increase the length/diameter ratio of β′ precipitate, and thus high density of slender precipitates are formed. It is supposed that Ag segregation limits the diffusional growth of the $\beta'_{Ag}$ precipitate along the cross-section. Therefore, the $\beta'_{Ag}$ phase with Ag segregation is much slender than the β′ phase formed in the base Al-Mg-Si alloy. As a consequence the strengthening of β′ phase will be influenced, as discussed in the next section. The schematic illustration of the influence of Ag segregation on the morphology evolution of precipitates is presented in Fig. 16. While for the β″ phase formed at the peak-aged stage, the influence of Ag segregation on the morphology of β″ phase is not evident. It is because of the Ag atoms partially replace the Al columns at the β″/α-Al interface, which could not effectively suppress the diffusional growth of β″ phase along the cross-section. The partial replacement of Ag atoms at the β″/ α-Al interface is shown in Supplementary Figure S3 and Supplementary Figure S4.

Ag has been known as one of the ‘magic’ microalloying elements in aluminum alloys since the 1960s [48, 49], accelerating precipitate phase nucleation or sometimes even changing the type of phase that forms.

Using electron microscopy and atom probe tomography, previous studies have shown that in this role Ag atoms participate within the precipitate phase [32, 50] or segregate at the precipitate/matrix interfaces [51]. However, the detailed mechanisms seem to vary from one alloy system to another. For instance, DFT calculations have shown that Ag atoms prefer to cluster on the close-packed planes within the aluminum matrix [52]. This intrinsic preference of $\{111\}_\alpha$ crystallographic planes explains the formation of a new ζ (AgAl) phase [52] and the Ag interfacial segregation on the γ′ ($Ag_2Al$) phase [53, 54] in the binary Al-Ag system. Indeed, Ag also co-clusters with Mg for various precipitates with their interfaces parallel to the $\{111\}_\alpha$ planes, including the Ω ($Al_2Cu$) phase in the Al-Cu-Mg-Ag system [36, 55, 56], the T1 ($Al_2CuLi$) phase in the Al-Cu-Li-Mg-Ag system [57, 58] and the η′/η ($Mg_2Zn$) phases in the Al-Zn-Mg-Ag system [59]. In contrast, Ag segregates as on $\{100\}_\alpha$ planes as bi-layers for the θ′ ($Al_2Cu$) phase in the Al-Cu-Ag system [60] and the phenomenon is more complex for the β″/β′ ($Mg_2Si$) [32], C and Q phases [50] in the Al-Mg-Si system. Together with previous work, our results demonstrate that DFT calculations are powerful in explaining the interfacial segregation, especially when combined with atomic resolution characterization. But the calculations up to now are still largely limited to each specific system, which calls for a further study to rationalize the microalloying mechanisms of the Ag in aluminum alloys in general.

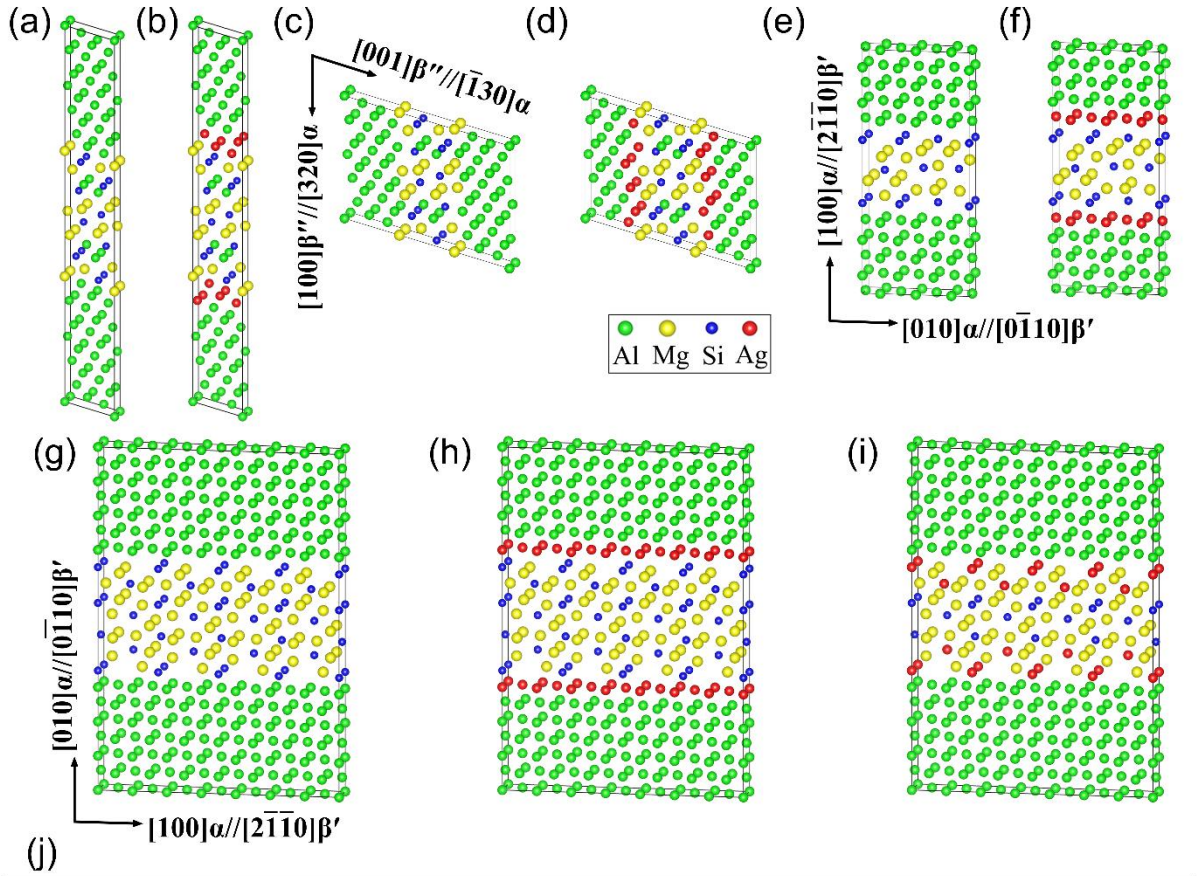


| | Structure | Number of atoms | Total energy (eV) | Formation enthalpy (eV/atom) | Ag segregation enthalpy (eV/Ag atom) |
|---|---|---|---|---|---|
| **(a)** | Mg11Al47Si8 | 66 | -236.14 | 0.012 | — |
| **(b)** | Mg11Al39Si8Ag8 | 66 | -230.13 | -0.0081 | -0.26 |
| **(c)** | Mg6Al23Si4 | 66 | -232.04 | 0.042 | — |
| **(d)** | Mg6Al17Si4Ag6 | 66 | -225.05 | -0.019 | -0.59 |
| **(e)** | Mg12Al54Si9 | 75 | -268.47 | 0.022 | — |
| **(f)** | Mg12Al42Si9Ag12 | 75 | -256.87 | 0.031 | -0.041 |
| **(g)** | Mg48Al182Si28 | 258 | -908.27 | 0.0065 | — |
| **(h)** | Mg56Al154Si28Ag28 | 266 | -901.03 | -0.015 | -0.29 |
| **(i)** | Mg48Al182Si12Ag16 | 258 | -869.25 | -0.0034 | -0.39 |

Fig. 15. Interface structural models of β″/α-Al and β′/α-Al interfaces before and after Ag segregation, (a, b) and (c, d) the models of β″/α-Al interfaces along the $[001]_{\beta''}$ // $[\bar{1}30]_{\alpha}$ and $[100]_{\beta''}$ // $[320]_{\alpha}$ directions, respectively. (e, f) the models of coherent β′/α-Al interfaces along the $[01\bar{1}0]_{\beta'}$ direction. (g-i) the models of semi-coherent β′/α-Al interfaces along the $[2\bar{1}\bar{1}0]_{\beta'}$ direction. (h) Ag occupies the Al atoms in FCC matrix, (i) Ag occupies the Si atoms in β′ precipitate. (j) the formation enthalpy (eV/atom) and segregation enthalpy (eV/Ag atom) plotted as a function of interfacial composition, calculated using VASP-PBE-GGA.

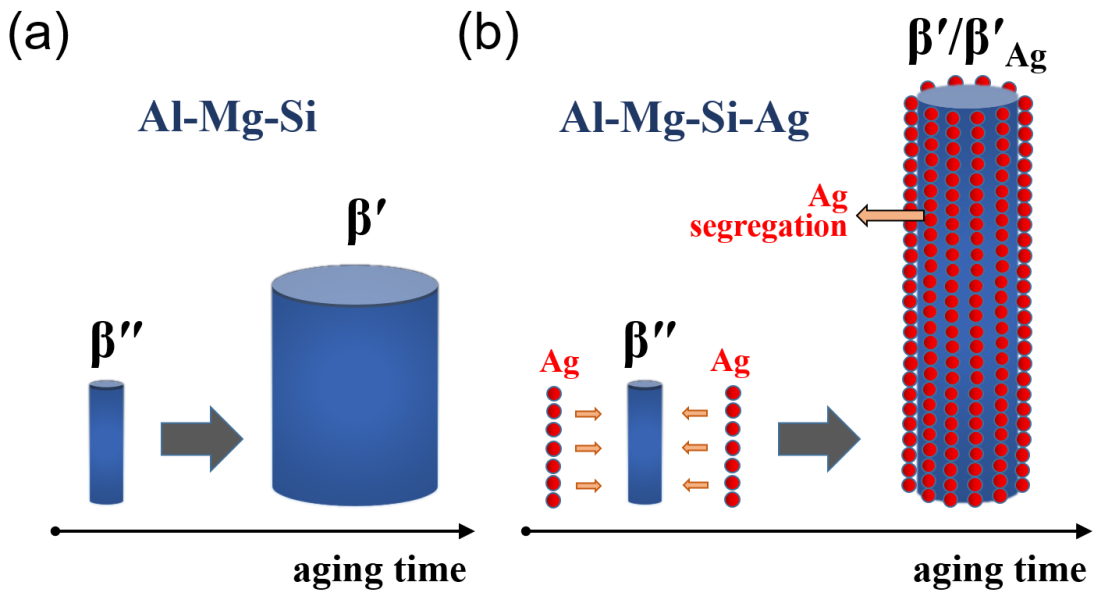


Fig. 16 Schematic illustration of the morphology evolution of precipitates in the investigated two alloys, (a) the base Al-Mg-Si alloy, (b) the Al-Mg-Si-Ag alloy.

## 4.3. Influence of morphology on the strengthening potential of precipitates

### 4.3.1. β″ precipitate

Precipitation hardening is an indispensable strengthening mechanism in Al-Mg-Si alloys. The β″ precipitate formed at the peak-aged stage is strengthening by shearing dislocation during deformation because of the small size and high coherency of these precipitates [61, 62]. The yield stress of β″ phase could be calculated by a model developed in reference [62]. The contribution to the yield stress from precipitation hardening can be summarized as:

$$\sigma_p = \frac{M\bar{F}}{bL} \tag{1}$$

where M is the Taylor factor (3.06 for FCC metals), and $b$ = 0.286 nm is the magnitude of the Burgers vector. $\bar{F}$ is the average obstacle strength of precipitate and $L$ is the average spacing of precipitate [62]. For the needle-like precipitate, the average spacing $L$ can be written as:

$$L = \left(\frac{2\pi}{f}\right)^{1/2} \bar{R} \tag{2}$$

where $f$ is the volume fraction of precipitate and $\bar{R}$ is the average radius of a needle-like precipitate. For the shearable precipitate, the strength of precipitate is proportional to the radius:

$$F = kGbR \quad (3)$$

where $k = b/R_c$ is a constant and $R_c$ is the radius at which the precipitate becomes nonshearable and is identified as 2.5 nm in reference [62], G = 28 GPa is the shear modulus of aluminum at room temperature, and R is the radius of precipitate. Substituting equation (2), (3) and the parameters into equation (1) results in the equation, $\sigma_p = 3.91 \times 10^3 (f^{\frac{1}{2}})$, implying that the volume fraction *f* plays an important role in shearable precipitation strengthening. Depending on the quantified details of β″ precipitate listed in Table 2, the yield stress of the A1 base alloy with shearable β″ precipitate can be calculated as 191.55 MPa, which is smaller than that of the Ag-added A2 alloy (217.70 MPa), which has denser and smaller β″ precipitate distribution. It is clear that Ag addition could improve the strengthening ability of β″ precipitate for the increased volume fraction of precipitate.

## 4.3.2. β′ precipitate

To reveal the quantitative effect of the morphology on the strengthening potential of β′ phase, the contribution of β′ phase to the yield strength is calculated for the two alloys. The nonshearable β′ phase is strengthening by bypass mechanism during deformation. The contribution of nonshearable particle to the strength of aluminum alloys has been evaluated in terms of the original or modified Orowan equations [63]. A.W. Zhu et al. [64] developed an appropriate version of the Orowan equation for aluminum alloys containing oriented <100>$_\alpha$ precipitate rods. For application to rod-like particles of diameter $D_r$, length $L_r$ (>>$D_r$) and volume fraction $f_v$, the yield stress for rod particle as:

$$\tau_p = 0.15G\frac{b}{D_r}(f_v^{1/2} + 1.84f_v + 1.84f_v^{3/2})\ln\frac{1.316D_r}{r_0} \quad (4)$$

$r_0$ is the inner cut-off radius for the calculation of the dislocation line tension and is 0.572 nm for aluminum alloys, and the volume fraction $f_v$ of β′ precipitate for the Al-Mg-Si alloys is calculated by:

$$f_v = \pi N_d L_r (\frac{D_r}{2})^2 \quad (5)$$

where $N_d$ is the number density of β′ precipitates.

In order to explore the relationship between the length/diameter ratio and strengthening ability of β′ precipitate, the number density ($N_d$) of β′ is intended as $4.0\times10^{-6}$ according to the experimental results. Setting the parameters of diameter $D_r$ and the length $L_r$ of precipitate as variable and the equation (4) could translate

to:

$$\tau_p = \left[2.13{L_r}^{\frac{1}{2}} + 6.94 \times 10^{-3} D_r L_r + 1.23 \times 10^{-5} {L_r}^{\frac{3}{2}} {D_r}^2\right](0.83 + \ln D_r) \quad (6)$$

According to experimental results, $D_r$ is varying from 0 to 10 nm and $L_r$ is varying from 50 to 300. The relationship among diameter ($D_r$), length $L_r$ and yield stress ($\tau_p$) is plotted in Fig. 17 (a), it could be seen that the yield strength is improved as the increase of the diameter and length. To reveal the relationship between the yield strength and length/diameter ratio, the $D_r$ is denoted as 5 nm (average $D_r$: $D_r$ = 5.02 nm for the A1 alloy, $D_r$ = 4.47 nm for the Ag-added A2 alloy), the equation (6) is transform to:

$$\tau_p = 11.61 \times \left(\frac{L_r}{D_r}\right)^{\frac{1}{2}} + 0.41 \times \left(\frac{L_r}{D_r}\right) + 8.39 \times 10^{-3} \cdot \left(\frac{L_r}{D_r}\right)^{\frac{3}{2}} \quad (7)$$

The $\tau_p$ plotted as a function of length/diameter ratio $L_r/D_r$, is shown in Fig. 17 (b). It could be seen that the $\tau_p$ is improved with increasing $L_r/D_r$, implying that the precipitate with higher length/diameter ratio has stronger strengthening ability. Ag addition changes the morphology of β′ precipitate from stubby to slender, leading to stronger strengthening ability. Traditionally, the precipitation hardening is increased by promoting the nucleation of precipitates, which leads to a smaller and denser precipitate distribution, the precipitation hardening can be promoted by changing the morphology of precipitates has not systematically investigated. The present finding that the yield strength can be increased by promoting the length/diameter ratio of precipitates provides an additional route for strengthening the alloy.

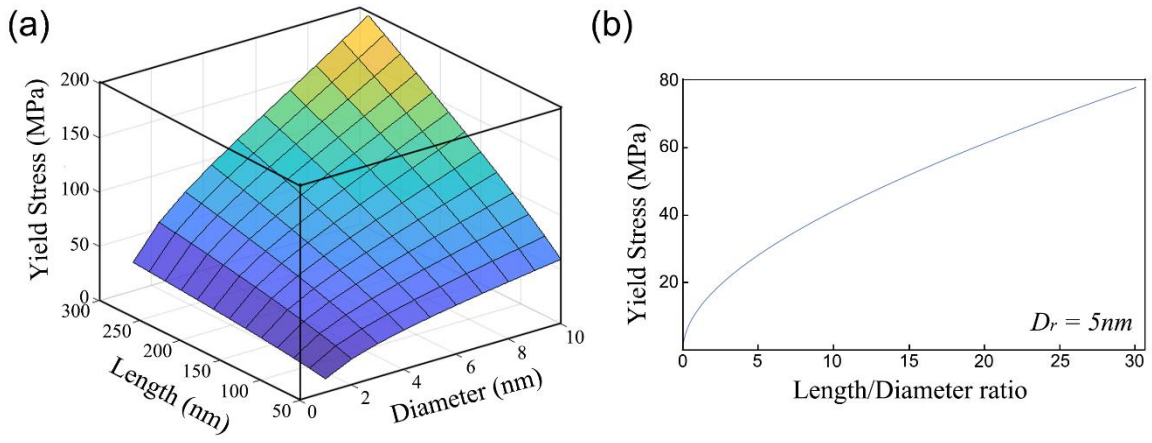


Fig. 17. (a) Yield stress $\tau_p$ plotted as a function of diameter $D_r$ and length $L_r$. (b) Yield stress $\tau_p$ plotted as a function of length/diameter ratio ($L_r/D_r$) with $D_r$ is fixed as 5 nm.

## 5. Conclusions

The effect of Ag addition on the precipitation evolution and interfacial segregation for Al-Mg-Si alloys was systematically investigated. Ag could not only change the atomic structure of precipitates and refine the distribution of precipitates, but also segregate at the precipitate/matrix interfaces and change the morphology of precipitate, which provides an additional strengthening potential.

1. At the early aging stage, Ag atoms enter the interior of clusters and form the Mg-Si-Ag co-clusters. At the peak aging stage, Ag atoms preferentially segregate at the GP zone/α-Al and β"/α-Al interfaces by replacing of Al atom in FCC matrix. Nearly no Ag is observed at the interior of precipitates.
2. With prolonged aging time, Ag atoms generally incorporate into the interior of β" precipitate, facilitating the formation of QP lattice and the local symmetry substructures, Ag sub-unit (1) and Ag sub-unit (2). The Ag sub-unit (1) transforms to $\beta'_{Ag}$ unit cell (i.e. $\beta'_{Ag1}$ and $\beta'_{Ag2}$.) and the Ag sub-unit (2) evolves into $Q'_{Ag}$ unit cell. All the precipitates in the over-aging stage have a composite and disordered structure due to the coexistence of different unit cells ($\beta'_{Ag1}$, $\beta'_{Ag2}$, $Q'_{Ag}$ and β′) and the non-periodic arrangement of Ag atoms within the precipitate.
3. At the equilibrium stage, Ag atoms incorporated in metastable precipitates release into the α-Al matrix or form the Ag particle. The precipitation sequence of Mg-rich Al-Mg-Si-Ag alloys can be identified as: SSSS → atomic clusters → β″ → $\beta'_{Ag1}$, $\beta'_{Ag2}$, $Q'_{Ag}$, β′ → β, Ag particle. In general, Ag atoms undergo a process of "segregate at the precipitate/matrix interface → incorporate into the interior of precipitate → release into the α-Al matrix" during the precipitation for Al-Mg-Si-Ag alloys.
4. Ag segregation is found at the interfaces of almost all metastable phases (including GP zones, β″, β′/ $\beta'_{Ag}$ phases) in Al-Mg-Si-Ag alloys. Ag segregation at the interfaces could increase the length/diameter ratio of β′ phase, and thus improve precipitate strengthening.

## Acknowledgments

This work was supported by the National Natural Science Foundation of China (Grant No. 51871035), the Fundamental Research Funds for the Central Universities of China (Grant No. 2018CDGFCL0002, 2019CDQYWL029), the Foundation for Innovative Research Groups of the National Natural Science Foundation of China (Grant No. 51421001), and the program of China Scholarships Council (No. 201706050125). The electron microscopy work was performed at the Electron Microscopy Center of Chongqing University, China. The authors also gratefully acknowledge the computational support from

Nikhil Medhekar at Monash University with computation resources from the National Computational Infrastructure and Pawsey Supercomputing Centre.

## References

[1] J. Hirsch, T. Al-Samman, Superior light metals by texture engineering: Optimized aluminum and magnesium alloys for automotive applications, Acta Mater. 61 (2013) 818-843.

[2] S. Pogatscher, H. Antrekowitsch, H. Leitner, T. Ebner, P.J. Uggowitzer, Mechanisms controlling the artificial aging of Al-Mg-Si Alloys, Acta Mater. 59 (2011) 3352-3363.

[3] W.S. Millera, L. Zhuanga, J. Bottemaa, A.J. Wittebrooda, P.D. Smetb, A. Haszlerc, A. Viereggec, Recent development in aluminium alloys for the automotive industry, Mater. Sci. Eng. A 280 (2000) 37-49.

[4] S.J. Andersen, H.W. Zandbergen, J. Jansen, C. TrÆholt, U. Tundal, O. Reiso, The crystal structure of the β″ phase in Al-Mg-Si alloys, Acta Mater. 46 (1998) 3283-3298.

[5] G.A. Edwards, K. Stille, G.L. Dunlop, M.J. Couper, The precipitation sequence in Al-Mg-Si alloys, Acta Mater. 46 (1998) 3893-3904.

[6] C. Cayron, P.A. Buffat, Transmission electron microscopy study of the β′ phase (Al-Mg-Si alloys) and QC phase (Al-Cu-Mg-Si alloys): ordering mechanism and crystallographic structure, Acta Mater. 48 (2000) 2639-2653.

[7] S.J. Andersen, C.D. Marioara, A. Frøseth, R. Vissers, H.W. Zandbergen, Crystal structure of the orthorhombic U2-Al4Mg4Si4 precipitate in the Al-Mg-Si alloy system and its relation to the β′ and β″ phases, Mater. Sci. Eng. A 390 (2005) 127-138.

[8] T. Saito, F.J.H. Ehlers, W. Lefebvre, D. Hernandez-Maldonado, R. Bjørge, C.D. Marioara, S.J. Andersen, R. Holmestad, HAADF-STEM and DFT investigations of the Zn-containing β″ phase in Al-Mg-Si alloys, Acta Mater. 78 (2014) 245-253.

[9] Y.X. Lai, B.C. Jiang, C.H. Liu, Z.K. Chen, C.L. Wu, J.H. Chen, Low-alloy-correlated reversal of the precipitation sequence in Al-Mg-Si alloys, J. Alloys Compd. 701 (2017) 94-98.

[10] K. Matsuda, Y. Sakaguchi, Y. Miyata, Y. Uetani, T. Sato, S.I. A. Kamio, Precipitation sequence of various kinds of metastable phases in Al-1.0mass% Mg2Si-0.4mass% Si alloy, J. Mater. Sci. 35 (2000) 179-189

[11] P.H. Ninive, A. Strandlie, S. Gulbrandsen-Dahl, W. Lefebvre, C.D. Marioara, S.J. Andersen, J. Friis, R. Holmestad, O.M. Løvvik, Detailed atomistic insight into the β″ phase in Al-Mg-Si alloys, Acta Mater. 69

(2014) 126-134.

[12] W. Yang, M. Wang, Y. Jia, R. Zhang, Studies of orientations of β″ precipitates in Al-Mg-Si-(Cu) alloys by electron diffraction and transition matrix analysis, Metall. Mater. Trans. A 42 (2011) 2917-2929.

[13] M.A. van Huis, J.H. Chen, M.H.F. Sluiter, H.W. Zandbergen, Phase stability and structural features of matrix-embedded hardening precipitates in Al-Mg-Si alloys in the early stages of evolution, Acta Mater. 55 (2007) 2183-2199.

[14] R. Vissers, M.A. van Huis, J. Jansen, H.W. Zandbergen, C.D. Marioara, S.J. Andersen, The crystal structure of the β′ phase in Al-Mg-Si alloys, Acta Mater. 55 (2007) 3815-3823.

[15] R.-K. Pan, L. Ma, N. Bian, M.-H. Wang, P.-B. Li, B.-Y. Tang, L.-M. Peng, W.-J. Ding, First-principles study on the elastic properties of B′ and Q phase in Al-Mg-Si (-Cu) alloys, Phys. Scr. 87 (2013) 015601.

[16] S.J. Andersen, C.D. Marioara, R. Vissers, A. Frøseth, H.W. Zandbergen, The structural relation between precipitates in Al-Mg-Si alloys, the Al-matrix and diamond silicon, with emphasis on the trigonal phase U1-MgAl2Si2, Mater. Sci. Eng. A 444 (2007) 157-169.

[17] E.A. Mørtsell, C.D. Marioara, S.J. Andersen, J. Røyset, O. Reiso, R. Holmestad, Effects of Germanium, Copper, and Silver Substitutions on Hardness and Microstructure in Lean Al-Mg-Si Alloys, Metall. Mater. Trans. A 46 (2015) 4369-4379.

[18] M.W. Zandbergen, A. Cerezo, G.D.W. Smith, Study of precipitation in Al-Mg-Si alloys by atom probe tomography II. Influence of Cu additions, Acta Mater. 101 (2015) 149-158.

[19] L.P. Ding, Z.H. Jia, Z.Q. Zhang, R.E. Sanders, Q. Liu, G. Yang, The natural aging and precipitation hardening behaviour of Al-Mg-Si-Cu alloys with different Mg/Si ratios and Cu additions, Mater. Sci. Eng. A 627 (2015) 119-126.

[20] J. Kim, E. Kobayashi, T. Sato, Effects of Cu addition on behavior of nanoclusters during multi-step aging in Al-Mg-Si alloys, Mater. Trans. 52 (2011) 906-913.

[21] C.D. Marioara, S.J. Andersen, T.N. Stene, H. Hasting, J. Walmsley, A.T.J. Van Helvoort, R. Holmestad, The effect of Cu on precipitation in Al-Mg-Si alloys, Philos. Mag. 87 (2007) 3385-3413.

[22] J. Buha, R.N. Lumley, A.G. Crosky, K. Hono, Secondary precipitation in an Al-Mg-Si-Cu alloy, Acta Mater. 55 (2007) 3015-3024.

[23] K.M. Ikeno, Y. Uetani, T. Sato, Metastable phases in an Al-Mg-Si alloy containing copper, Metall. Mater. Trans. A 32 (2001) 1293-1299.

[24] M. Torsæter, W. Lefebvre, C.D. Marioara, S.J. Andersen, J.C. Walmsley, R. Holmestad, Study of

intergrown L and Q′ precipitates in Al-Mg-Si-Cu alloys, Scr. Mater. 64 (2011) 817-820.

[25] W. Yang, M. Wang, X. Sheng, Q. Zhang, L. Huang, Precipitate characteristics and selected area diffraction patterns of the β′ and Q′ precipitates in Al-Mg-Si-Cu alloys, Philos. Mag. Lett. 91 (2011) 150-160.

[26] L. Ding, Z. Jia, J.-f. Nie, Y. Weng, L. Cao, H. Chen, X. Wu, Q. Liu, The structural and compositional evolution of precipitates in Al-Mg-Si-Cu alloy, Acta Mater. 145 (2018) 437-450.

[27] A.M. Ali, A.-F. Gaber, K. Matsuda, S. Ikeno, The structure and kinetics of the nanoscale precipitation processes in Al-1.0 wt pct Mg2Si-0.4 wt pct Mg-0.5 wt pct Ag alloy, Metall. Mater. Trans. A 44 (2013) 5234-5240.

[28] H. Zhang, Z. Zheng, Y. Lin, X. Luo, J. Zhong, Effects of Ag addition on the microstructure and thermal stability of 6156 alloy, J. Mater. Sci. 47 (2012) 4101-4109.

[29] Y. Weng, Z. Jia, L. Ding, Y. Pan, Y. Liu, Q. Liu, Effect of Ag and Cu additions on natural aging and precipitation hardening behavior in Al-Mg-Si alloys, J. Alloys Compd. 695 (2017) 2444-2452.

[30] T. Saito, E.A. Mørtsell, S. Wenner, C.D. Marioara, S.J. Andersen, J. Friis, K. Matsuda, R. Holmestad, Atomic structures of precipitates in Al-Mg-Si alloys with small additions of other elements, Adv. Eng. Mater. 20 (2018) 1800125.

[31] Y. Weng, Z. Jia, L. Ding, S. Muraishi, Q. Liu, Clustering behavior during natural aging and artificial aging in Al-Mg-Si alloys with different Ag and Cu addition, Mater. Sci. Eng. A 732 (2018) 273-283.

[32] C.D. Marioara, J. Nakamura, K. Matsuda, S.J. Andersen, R. Holmestad, T. Sato, T. Kawabata, S. Ikeno, HAADF-STEM study of β′-type precipitates in an over-aged Al-Mg-Si-Ag alloy, Philos. Mag. 92 (2012) 1149-1158.

[33] K. Matsuda, S. Ikeno, T. Sato, Y. Uetani, New quaternary grain boundary precipitate in Al-Mg-Si alloy containing silver, Scr. Mater. 55 (2006) 127-129.

[34] E.A. Mørtsell, S.J. Andersen, J. Friis, C.D. Marioara, R. Holmestad, Atomistic details of precipitates in lean Al-Mg-Si alloys with trace additions of Ag and Ge studied by HAADF-STEM and DFT, Philos. Mag. 97 (2017) 851-866.

[35] J.M. Rosalie, L. Bourgeois, Silver segregation to θ′ (Al2Cu)-Al interfaces in Al-Cu-Ag alloys, Acta Mater. 60 (2012) 6033-6041.

[36] S.J. Kang, Y.-W. Kim, M. Kim, J.-M. Zuo, Determination of interfacial atomic structure, misfits and energetics of Ω phase in Al-Cu-Mg-Ag alloy, Acta Mater. 81 (2014) 501-511.

[37] M.A. van Huis, J.H. Chen, H.W. Zandbergen, M.H.F. Sluiter, Phase stability and structural relations of

nanometer-sized, matrix-embedded precipitate phases in Al-Mg-Si alloys in the late stages of evolution, Acta Mater. 54 (2006) 2945-2955.

[38] J.P. Perdew, K. Burke, M. Ernzerhof, Generalized Gradient Approximation Made Simple, Phys. Rev. Lett. 77 (1996) 3865-3868.

[39] P.E. Blochl, Projector augmented-wave method, Phys. Rev. B 50 (1994) 17953-17979.

[40] G. Kresse, D. Joubert, From ultrasoft pseudopotentials to the projector augmented-wave method, Phys. Rev. B 59 (1999) 1758-1775.

[41] G. Kresse, J. Furthmüller, Efficient iterative schemes for ab initio total-energy calculations using a plane-wave basis set, Phys. Rev. B, 54 (1996) 11169-11186.

[42] M. Methfessel, A.T. Paxton, High-precision sampling for Brillouin-zone integration in metals, Phys. Rev. B 1989; 40: 3616-3621.

[43] P.E. Blochl, O. Jepsen, O.K. Andersen, Improved tetrahedron method for Brillouin-zone integrations[J], Physical review. B, Condensed matter, 49 (1994) 16223-16233.

[44] K. Mathew, J.H. Montoya, A. Faghaninia, S. Dwarakanath, M. Aykol, H. Tang, I.-h. Chu, T. Smidt, B. Bocklund, M. Horton, J. Dagdelen, B. Wood, Z.-K. Liu, J. Neaton, S.P. Ong, K. Persson, A. Jain, Atomate: A high-level interface to generate, execute, and analyze computational materials science workflows, Comput. Mater. Sci. 139 (2017) 140-152.

[45] K. Matsuda, T. Naoi, K. Fujii, Y. Uetanib, T. Satoc, A. Kamioc, S. Ikenoa, Crystal structure of the β″ phase in an Al-1.0mass%Mg2Si-0.4mass%Si alloy, Mater. Sci. Eng. A 262 (1999) 232-237.

[46] W. Yang, M. Wang, R. Zhang, Q. Zhang, X. Sheng, The diffraction patterns from β″ precipitates in 12 orientations in Al-Mg-Si alloy, Scr. Mater. 62 (2010) 705-708.

[47] Y. Weng, Z. Jia, L. Ding, S. Muraishi, X. Wu, Q. Liu, The multiple orientation relationships and morphology of β' phase in Al-Mg-Si-Cu alloy, J. Alloys Compd. 767 (2018) 81-89.

[48] I.J. Polmear, A trace element effect in alloys based on the aluminium-zinc-magnesium system, Nature, 186 (1960) 303-304.

[49] J.H. Auld, J.T. Vietz, I.J. Polmear, T-phase precipitation induced by the addition of silver to an aluminium-copper-magnesium alloy, Nature, 209 (1966) 703-704.

[50] S. Wenner, C.D. Marioara, Q.M. Ramasse, D.-M. Kepaptsoglou, F.S. Hage, R. Holmestad, Atomic-resolution electron energy loss studies of precipitates in an Al-Mg-Si-Cu-Ag alloy, Scr. Mater. 74 (2014) 92-95.

[51] L. Reich, M. Murayama, K. Hono, Evolution of Ω phase in an Al-Cu-Mg-Ag alloy-a three-dimensional atom probe study, Acta Metall. 46 (1998) 6053-6062.

[52] Z. Zhang, L. Bourgeois, J.M. Rosalie, N.V. Medhekar, The bi-layered precipitate phase ζ in the Al-Ag alloy system, Acta Mater. 132 (2017) 525-537.

[53] Z. Zhang, J.M. Rosalie, N.V. Medhekar, L. Bourgeois, Resolving the FCC/HCP interfaces of the γ' (Ag2Al) precipitate phase in aluminium, Acta Mater. 174 (2019) 116-130.

[54] J.M. Rosalie, C. Dwyer, L. Bourgeois, On chemical order and interfacial segregation in γ′(AlAg2) precipitates, Acta Mater. 69 (2014) 224-235.

[55] J.M. Howe, Analytical transmission electron microscopy analysis of Ag and Mg segregation to {111} θ precipitate plates in an Al-Cu-Mg-Ag alloy, Philos. Mag. Lett. 70 (1994) 111-120.

[56] C.R. Hutchinson, X. Fan, S.J. Pennycook, G.J. Shiflet, On the origin of the high coarsening resistance of Ω plates in Al-Cu-Mg-Ag alloys, Acta mater. 49 (2001) 2827-2841.

[57] V. Araullo-Peters, B. Gault, F.d. Geuser, A. Deschamps, J.M. Cairney, Microstructural evolution during ageing of Al-Cu-Li-x alloys, Acta Mater. 66 (2014) 199-208.

[58] S.J. Kang, T.-H. Kim, C.-W. Yang, J.I. Lee, E.S. Park, T.W. Noh, M. Kim, Atomic structure and growth mechanism of T1 precipitate in Al-Cu-Li-Mg-Ag alloy, Scr. Mater. 109 (2015) 68-71.

[59] C.E. Macchi, A. Somoza, A. Dupasquier, I.J. Polmear, Secondary precipitation in Al-Zn-Mg-(Ag) alloys, Acta Mater. 51 (2003) 5151-5158.

[60] J.M. Rosalie, L. Bourgeois, Silver segregation to θ′ (Al2Cu)-Al interfaces in Al-Cu-Ag alloys, Acta Mater. 60 (2012) 6033-6041.

[61] W.J. Poole, X. Wang, D.J. Lloyd, J.D. Embury, The shearable-non-shearable transition in Al-Mg-Si-Cu precipitation hardening alloys: implications on the distribution of slip, work hardening and fracture, Philos. Mag. 85 (2005) 3113-3135.

[62] X. Wang, W.J. Poole, S. Esmaeili, D.J. Lloyd, J.D. Embury, Precipitation Strengthening of the Aluminum Alloy AA6111, Metall. Mater. Trans. A 34 (2003) 2913-2924.

[63] M.F.Ashby, Results and consequences of a recalculation of the frank-read and the orowan stress, Acta Metall. 14 (1966) 679-681.

[64] A.W. Zhu, E.A.S. Jr, Strengthening effect of unshearable particles of finite size: a computer experiment study, Acta Mater. 47 (1999) 3263-3269.

## Figure captions

Fig. 1. Evolution of Vickers hardness for the two investigated alloys during AA at 170 °C immediately after water quenching.

Fig. 2. TEM bright-field images of the two alloys aged at 170 °C for different times. (a) A1, 5h peak aging, (b) A1, 2 days AA, (c) A1, 1 week AA, (d) A2, 2h peak aging, (e) A2, 2 days AA, (f) A2, 1 week AA.

Fig. 3. (a) HAADF-STEM image of β″ precipitate formed at 5h peak aging for the A1 base alloy, (c) HAADF-STEM image of β′ precipitate formed at one week over aging for the A1 base alloy. (b, d) corresponding FFT patterns of (a, c), respectively. The unit cells of β″ and β′ are marked by red lines.

Fig. 4. Precipitate length distribution of β″ and β′ precipitates for the two alloys, (a) β″, peak aging, (b) β′, one week AA.

Fig. 5. (a) Atoms maps for the Ag-added A2 alloy after AA at 170 °C for 5 min, (b) the enlarged 3DAP maps of the zone b marked in (a), (c) frequency histograms (experimental in black and randomly labelled in red) of 5NN distance between Mg, Si and Cu solute atoms, (d) the measured Ag/Mg ratio plotted against the cluster size.

Fig. 6. (a, b, c, d) HAADF-STEM images of GP zone and β″ phases formed in the peak-aged condition (170 °C for 2h) for the Ag-added A2 alloy, (a) GP zone, (b, c, d) β″ phase. (e, f, g, h) the corresponding FFT patterns of (a, b, c, d), respectively. The β″, U2 and β′ cell units are marked by the red, yellow and purple lines, respectively. The low density cylinder (LDC) is marked by the dashed red circle.

Fig. 7. (a, e) HAADF-STEM images of β″ and $Q'_{Ag}$ phases formed at the over-aged condition (170 °C for 2 d) for the Ag-added A2 alloy. (b, f) the corresponding FFT patterns of (a, e), respectively. (c, g) the enlarged HAADF-STEM images of the zone c and g marked in (a and e), respectively. The QP lattice is marked by dashed green lines. (d, h) the enlarged HAADF-STEM images of the zone d and h marked in (c, g), respectively. The β″ and $Q'_{Ag}$ unit cells are marked by the red and yellow lines, respectively.

Fig. 8. (a, b, c, d) HAADF-STEM images of four individual $\beta'_{Ag}$ precipitates formed after one week AA for the Ag-added A2 alloy, (e, f, g, h) the corresponding FFT patterns of (a, b, c, d), respectively. The β′ and $\beta'_{Ag}$ unit cells are marked by red lines.

Fig. 9. (a, d) HAADF-STEM images of $\beta'_{Ag}$ precipitates formed at the over-aged condition (170 °C for one week). (b) the corresponding FFT pattern of (a). (c, f, h, i) the enlarged HAADF-STEM images of the zones marked in (a). (e) the enlarged HAADF-STEM image of the zone marked in (d). (g) schematic illustration of

the β′ unit cell. The $\beta'_{Ag}$ cell unit is marked by the red lines. The QP lattice and Ag-network are marked by dashed green and yellow lines, respectively.

Fig. 10. (a, d) HAADF-STEM images of $\beta'_{Ag}$ precipitates formed at the over-aged condition (170 $^{o}$C for one week). (b, c) and (e, f) are the enlarged HAADF-STEM images of the zones marked in (a) and (d), respectively. The QP lattice and Al matrix are marked by dashed green and yellow lines, respectively. The β′ cell unit is marked by the red lines.

Fig. 11. (a) HAADF-STEM image of the Ag-added A2 alloy at an equilibrium stage (300 $^{o}$C AA for two weeks). (b-e) STEM-EDS maps of (a), (f) HAADF-STEM image of Ag particle, (g-j) STEM-EDS maps of (f).

Fig. 12. Formation enthalpy △H (eV/atom) plotted as a function of composition, calculated using VASP-PW-GGA.

Fig. 13. Contour maps of the electron densities of three phases on different planes calculated using VASP-PW-GGA. (a) $\beta'_{Ag2}$, (001), Z = 0Å, (b) $\beta'_{Ag1}$, (010), Z = 2Å, (c) $Q'_{Ag}$, (001), Z = 0Å, (d) $Q'_{Ag}$, (110), Z = 6Å. The strong covalent bonding between Ag-Al and Ag-Si bonds in $\beta'_{Ag}$ and $Q'_{Ag}$ is displayed by dashed red and blue circles, respectively.

Fig. 14. Schematic illustration of the precipitate evolution in the Mg-rich Al-Mg-Si-Ag alloy.

Fig. 15. Interface structural models of β″/α-Al and β′/α-Al interfaces before and after Ag segregation, (a, b) and (c, d) the models of β″/α-Al interfaces along the $[001]_{\beta''}$ // $[\bar{1}30]_{\alpha}$ and $[100]_{\beta''}$ // $[320]_{\alpha}$ directions, respectively. (e, f) the models of coherent β′/α-Al interfaces along the $[01\bar{1}0]_{\beta'}$ direction. (g-i) the models of semi-coherent β′/α-Al interfaces along the $[2\bar{1}\bar{1}0]_{\beta'}$ direction. (h) Ag occupies the Al atoms in FCC matrix, (i) Ag occupies the Si atoms in β′ precipitate. (j) the formation enthalpy (eV/atom) and segregation enthalpy (eV/Ag atom) plotted as a function of interfacial composition, calculated using VASP-PBE-GGA.

Fig. 16 Schematic illustration of the morphology evolution of precipitates in the investigated two alloys, (a) the base Al-Mg-Si alloy, (b) the Al-Mg-Si-Ag alloy.

Fig. 17. (a) Yield stress $\tau_p$ plotted as a function of diameter $D_r$ and length $L_r$. (b) Yield stress $\tau_p$ plotted as a function of length/diameter ratio ($L_r/D_r$) with $D_r$ is fixed as 5 nm.

## Table captions

Table 1 Chemical compositions of the two investigated alloys

Table 2 Statistics of β″ and β′ precipitates for the two alloys after AA at different aging times.

Table 3 Comparison between the crystal structure of β′, $\beta'_{Ag1}$ and $\beta'_{Ag2}$ unit cells.